AGU PUBLICATIONS

JGR

Journal of Geophysical Research: Earth Surface

RESEARCH ARTICLE

10.1002/2016JF003823

Key Points:
- Storms trigger the formation of shoals on ebb-tidal deltas
- A local imbalance between the bathymetry and wave conditions causes shoals to grow
- Shoal migration speed increases with increasing incident wave energy and decreasing tidal prism

Supporting Information:
- Supporting Information S1
- Data S1
- Movie S1
- Movie S2
- Movie S3

Correspondence to:
W. Ridderinkhof,
wim.ridderinkhof@gmail.com

Citation:
Ridderinkhof, W., H. E. de Swart, M. van der Vegt, and P. Hoekstra (2016), Modeling the growth and migration of sandy shoals on ebb-tidal deltas, *J. Geophys. Res. Earth Surf.*, *121*, 1351–1372, doi:10.1002/2016JF003823.

Received 12 JAN 2016
Accepted 30 JUN 2016
Accepted article online 12 JUL 2016
Published online 25 JUL 2016

Modeling the growth and migration of sandy shoals on ebb-tidal deltas

W. Ridderinkhof[1], H. E. de Swart[1], M. van der Vegt[1], and P. Hoekstra[1]

[1]Institute for Marine and Atmospheric Research, Utrecht University, Utrecht, Netherlands

Abstract Coherent sandy shoals that migrate toward the downdrift coast are observed on many ebb-tidal deltas. In this study, processes that cause the growth and migration of shoals on ebb-tidal deltas are identified. Moreover, the effect of the incident wave energy and the tidal prism of an inlet on the migration speed of these shoals is investigated. For this, a numerical morphodynamic model with an idealized geometric setup is employed. The model computes the bed level evolution due to local erosion and deposition of sand driven by tides and waves. Analysis of model results shows that shoals grow when there is a local imbalance between the bathymetry and the wave conditions, which in this study was imposed by manually breaching the ebb-tidal delta or by adding storms to the wave forcing. There are thresholds for shoal formation that depend on the distribution of the sand and the incident wave energy. Wave refraction over the shoals leads to focusing of wave energy and increased wave energy dissipation around the location of the local minimum water depth. This generates residual currents over the shoal and increased skin friction toward the local minimum water depth, which together create a sand transport pattern that induces the growth and migration of the shoal. Sand transport due to asymmetric waves contributes to keeping the shoal a coherent structure. The shoal migration speed increases with increasing incident wave energy and decreasing tidal prism; this is because tidal residual currents oppose the wave-driven residual currents that cause shoal migration.

1. Introduction

There is a strong coupling between the sand balance of the nearshore zone of barrier islands and processes that occur in and seaward of the tidal inlets that separate them. Seaward of inlets, sand is stored in ebb-tidal deltas [*Oertel*, 1975; *Walton and Adams*, 1976], as a result of the joint action of waves and tidal currents [*Hayes*, 1975; *Hayes and FitGerald*, 2013]. On many ebb-tidal deltas, shoals form repetitively and migrate toward the downdrift coast, i.e., in the direction of the net alongshore sediment transport [e.g., *Robinson*, 1975; *O'Connor et al.*, 2011]. These shoals play an important role in the sediment balance of the nearshore zone, as an attachment of a shoal may supply the coast with $\mathcal{O}(10^6)$ m^3 of sand [*Hofstede*, 1999].

Various generic conceptual models that describe the migration of shoals on ebb-tidal deltas have been introduced (Figure 1). These models [*FitzGerald*, 1982, 1988] distinguish between the stability of the main ebb channel. Sometimes the main ebb channel of an ebb-tidal delta is stable (i.e., it does not migrate); this is often due to the presence of layers that are resistent to erosion [*FitzGerald et al.*, 2000]. Wave built accumulations of sand on the margins of such ebb-tidal deltas cause formation and migration of shoals. These processes are referred to as stable inlet processes [*FitzGerald*, 1988]. At ebb-tidal deltas of other inlets, shoals form due to the accumulation of sand updrift of a channel. These shoals deflect the channel toward the downdrift coast until a breach occurs that establishes a more efficient ebb channel, and a large volume of sand is then located downdrift of the new channel. Part of this sand will fill up the old channel, and a part will form a shoal that migrates toward the downdrift coast. This process is referred to as ebb-tidal delta breaching [*FitzGerald*, 1988] or when it is limited to the seaward end of the channels on the ebb-tidal delta outerchannel shifting [*FitzGerald et al.*, 2000].

Numerical model studies were conducted to gain insight into the physics that control the morphodynamics of ebb-tidal deltas. Migrating shoals on ebb-tidal deltas were for the first time modeled by *Cayocca* [2001] in simulations of the long-term morphologic evolution of the Arcachon inlet. A key conclusion was that waves are essential for the migration of shoals. *Siegle et al.* [2004] and *Elias et al.* [2006] performed case studies of the sand transport on ebb-tidal deltas and found sand recirculating in patterns where tidally driven offshore sand

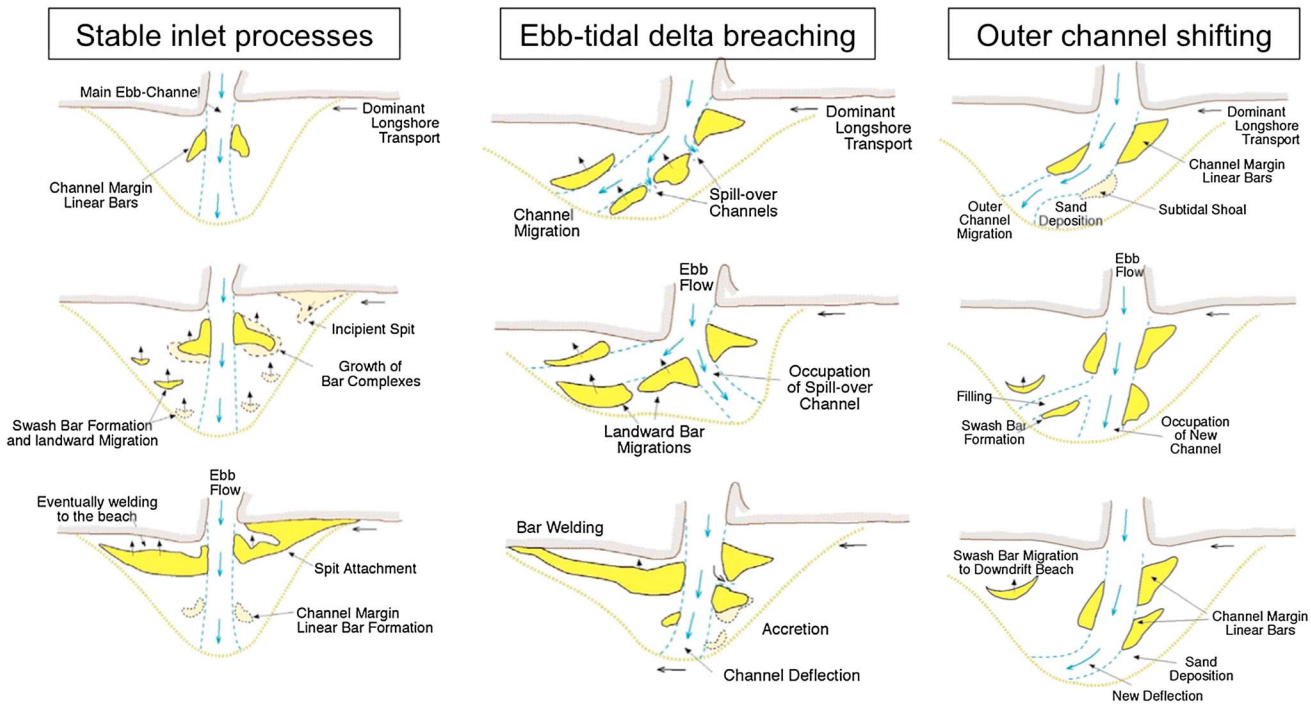

Figure 1. After *FitzGerald et al.* [2000]. Conceptual models of shoal formation and migration on ebb-tidal deltas.

transport takes place in the ebb channel and primarily wave-driven onshore sand transport over the margins of the ebb-tidal delta. *Herrling and Winter* [2014] showed that sand also bypasses ebb-tidal deltas without forming coherent bodies and that sand transport patterns under high-energy wave conditions are different from those under fair weather conditions.

Ranasinghe and Pattiaratchi [2003] and *Bertin et al.* [2009a] assessed physical mechanisms that cause the seasonal closure of inlets by shoals, but their conclusions were different. *Ranasinghe and Pattiaratchi* [2003] used representative forcing conditions for Australian inlets and found that cross-shore sand transport due to asymmetric waves is a dominant mechanism that pushes sand toward the inlet and causes it to close. Asymmetric waves were also shown to be the cause of shoreward migration of sandbars on closed coasts [e.g., *Hoefel and Elgar*, 2003; *Ruessink et al.*, 2007]. On the other hand, *Bertin et al.* [2009a] related the movement of shoals that cause the closure of a Portugese inlet to wave-driven residual flow over the shoal that is caused by the imbalance between the onshore component of the wave radiation stress and pressure gradients. In that study, sand transport due to asymmetric waves was not considered.

Nahon et al. [2012] and *Dastgheib* [2012] successfully simulated migrating shoals that resemble those in the conceptual models of *FitzGerald* [1988]. Both assessed how the morphological behavior of a tidal inlet system depends on the forcing of tides and waves. In their simulations (in which wave height was kept constant), formation and migration of shoals on ebb-tidal deltas only occurred when they considered high-energy wave conditions ($H_s \sim 2$ m). Interestingly, *Nahon et al.* [2012] obtained a time period of ~18 weeks between consecutive shoals, whereas *Dastgheib* [2012] obtained a period of ~15–20 years. A possible explanation for this difference is that tidal prism in the latter study was much larger ($\mathcal{O}(10^8)$ m^3 versus $\mathcal{O}(10^7)$ m^3), since observations indicate that the tidal prism is positively related to the period between consecutive shoals and negatively related to the migration speed of shoals on ebb-tidal deltas [*Gaudiano and Kana*, 2001; *Ridderinkhof et al.*, 2016]. Although *Nahon et al.* [2012] and *Dastgheib* [2012] simulated the generation and migration of these shoals, they did not discuss underlying physical mechanisms.

This study has two specific aims. The first is to investigate what conditions are necessary and sufficient to allow for the growth of a shoal on an ebb-tidal delta and what conditions are required for shoal migration. The hypothesis is that shoals are transient phenomena that are generated when a part of the ebb-tidal delta bathymetry is locally out of equilibrium with the wave conditions. This is inspired by the conditions responsible for the transformation of the morphology of sandbars, i.e., cross-shore bar migration and longshore

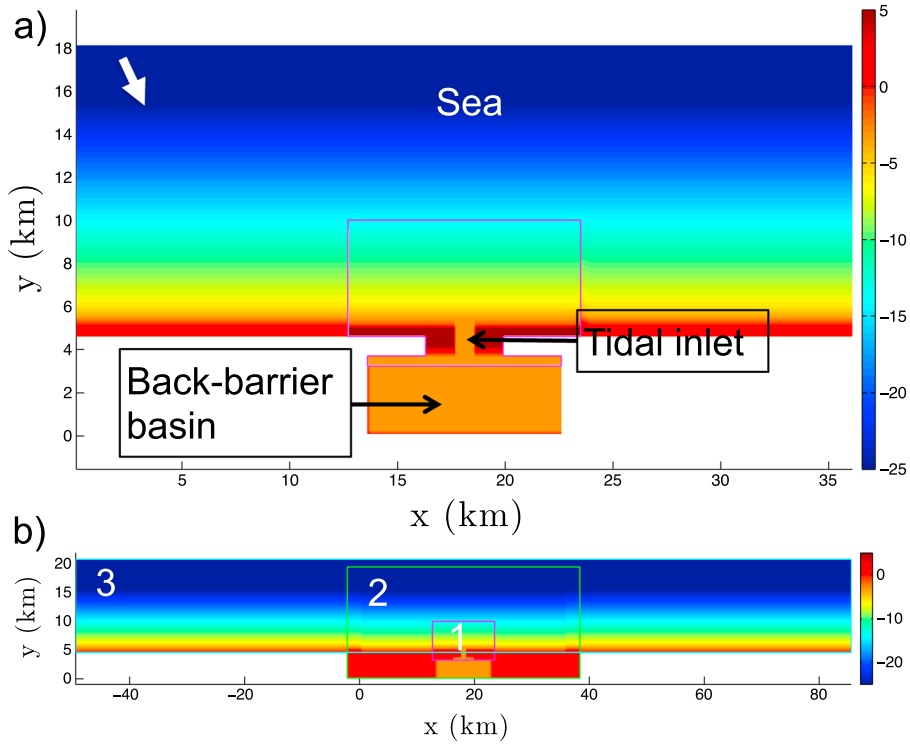

Figure 2. (a) Domain that is considered in the Delft3D model with colors indicating water depth (m). The *magenta lines* indicate the borders of the region in which the model has the highest resolution. The white arrow indicates the propagation direction of the incoming waves. (b) Domain that is considered in the SWAN model, which consists of three nested grids indicated by *white numbers*.

variability [*Lippman and Holman*, 1990]. It will also be discussed which physical processes contribute to the growth and migration of shoals. The second aim is to determine the relationship between the migration speed of a shoal on an ebb-tidal delta and both the wave height and the tidal prism. As numerical studies showed that waves are important drivers of sediment transport on ebb-tidal deltas, it is expected that shoals migrate faster over ebb-tidal deltas that are exposed to higher wave energy.

2. Material and Methods

To fulfill the objectives, the model Delft3D (as discussed by *Lesser et al.* [2004]) is employed together with the spectral wave model SWAN (extensively described by *Booij et al.* [1999] and *Holthuijsen* [2007]) to form a morphodynamic model with modules for currents, waves, sediment transport, and bed evolution. As is common practice in modeling studies of ebb-tidal deltas, the model is executed in a depth-averaged mode because this is computationally more efficient and has not led to significantly different results in this kind of environments than 3-D models [e.g., *Grunnet et al.*, 2004; *Lesser et al.*, 2004; *Fiechter et al.*, 2006]. Below, the applied depth-averaged version of the model is presented.

2.1. Morphodynamic Model

2.1.1. Model Domain

The morphodynamic module is employed on a domain (Figure 2a) that consists of a tidal inlet (size: 800 m by 1.3 km), which connects a back-barrier basin (size: 9 km by 3.5 km) to an open sea (size: 36 km by 13.5 km). Here *x* and *y* are the alongshore and cross-shore coordinates, respectively. The reason for considering a basin with these dimensions is that the ebb-tidal delta will be relatively small and a high resolution can be applied without too high computational costs. The model setup is inspired by the morphology and hydrodynamics of the Wadden Sea, a barrier island system in the southeastern part of the North Sea [see, e.g., *Ehlers*, 1988]. The dimensions of the modeled back-barrier basin are slightly larger than those of the smallest drainage basin of the Wadden Sea (Wichter Ee inlet system). The schematized wave conditions are based upon a wave buoy that is located seaward of the island Schiermonnikoog, recording wave height, period, and direction.

2.1.2. Currents

The currents are described by the depth-averaged shallow water equations,

$$\frac{\partial h}{\partial t} + \frac{\partial (hu)}{\partial x} + \frac{\partial (hv)}{\partial y} = 0, \tag{1}$$

$$\frac{\partial u}{\partial t} + u\frac{\partial u}{\partial x} + v\frac{\partial u}{\partial y} - fv = -g\frac{\partial \eta}{\partial x} - \frac{\tau_x}{\rho h} + \\ + \frac{1}{h}\left[\frac{\partial}{\partial x}\left(\nu_e h\frac{\partial u}{\partial x}\right) + \frac{\partial}{\partial y}\left(\nu_e h\frac{\partial u}{\partial y}\right)\right] + \frac{F_x}{\rho h}, \tag{2}$$

$$\frac{\partial v}{\partial t} + u\frac{\partial v}{\partial x} + v\frac{\partial v}{\partial y} + fu = -g\frac{\partial \eta}{\partial y} - \frac{\tau_y}{\rho h} + \\ + \frac{1}{h}\left[\frac{\partial}{\partial x}\left(\nu_e h\frac{\partial v}{\partial x}\right) + \frac{\partial}{\partial y}\left(\nu_e h\frac{\partial v}{\partial y}\right)\right] + \frac{F_y}{\rho h}. \tag{3}$$

Here h is the local water depth; η is the sea surface elevation with respect to the undisturbed water level; u and v are the depth-averaged velocities in the x and y direction, respectively; f is the Coriolis parameter; g is the acceleration due to gravity; ρ is the constant density of water; ν_e is the horizontal eddy viscosity, here assumed to be spatially uniform; and F_x, F_y are components of the wave-induced force per surface area, given by minus the divergence of the radiation stress tensor $\bar{\bar{S}}$ [*Longuet-Higgins and Stewart*, 1962], i.e.,

$$F_x = -\frac{\partial S_{xx}}{\partial x} - \frac{\partial S_{xy}}{\partial y}, \tag{4a}$$

$$F_y = -\frac{\partial S_{yx}}{\partial x} - \frac{\partial S_{yy}}{\partial y}, \tag{4b}$$

where $\bar{\bar{S}}$, with elements $S_{i,j}$, and $i, j = x$ or y, is provided by the wave module. The bed-shear stress components, τ_x and τ_y result from the nonlinear combination of the bed-shear stress vector due to currents, $\vec{\tau}_c$, and that due to waves, $\vec{\tau}_w$, which are combined with the parameterization of *Soulsby et al.* [1993] and the model of *Fredsoe* [1984]. Here $\vec{\tau}_w$ is controlled by the near-bed horizontal wave orbital velocity vector, which is determined using linear wave theory and the local wave height, wave period, and wave length as provided by the wave module. Furthermore, $\vec{\tau}_c$ is proportional to $|\vec{u}|\vec{u}$ (where $\vec{u} = (u, v)$), and is obtained with use of the formulation of *Colebrook and White* [1937] for the drag coefficient, with a roughness height that follows from *van Rijn* [2007a].

The tides are forced by a semidiurnal tidal wave (amplitude A, frequency ω_{M2}) that travels in the positive x direction in the open sea. This is achieved by forcing the alongshore open boundary with a harmonic variation in sea surface height and the cross-shore boundaries with harmonic Neumann conditions [*Roelvink and Walstra*, 2004].

2.1.3. Waves

The wave model SWAN is an open source third-generation spectral wave model [*Holthuijsen*, 2007]. It computes the wave spectrum in a domain using the wave action balance equation, which in this study is used in its stationary form

$$\frac{\partial (c_{g,x}N)}{\partial x} + \frac{\partial (c_{g,y}N)}{\partial y} + \frac{\partial (c_\theta N)}{\partial \theta} + \frac{\partial (c_\sigma N)}{\partial \sigma} = \frac{S}{\sigma}. \tag{5}$$

Here N is the spectral action density, which is a conserved quantity in the presence of currents, σ is the relative frequency, θ is the spectral direction, and $c_{g,x}$ and $c_{g,y}$ are the components of the wave group velocity vector $\vec{c}_g$ in the x and y direction, respectively. Furthermore, c_θ and c_σ are propagation velocities in the spectral space. Moreover, S represents all sources and sinks that generate, dissipate, or redistribute wave energy. The first two terms on the left-hand side of equation (5) thus describe the propagation of wave action in geographical space, the third term describes refraction due to spatial variations of the depth and the currents, and the fourth term describes the shifting of the relative frequency spectrum of the waves due to variations in depth and current. Finally, the sources and sinks that are considered in this study are bottom friction (formulation based

on Joint North Sea Wave Project (JONSWAP) model by *Hasselmann et al.* [1973]), white capping (formulation based on *Hasselmann et al.* [1973] and *Komen et al.* [1984]), and wave breaking (formulation based upon the dissipation of a bore [*Battjes and Janssen*, 1978], $\gamma = 0.73$).

The radiation stress tensor $\bar{\bar{S}}$ used in the morphodynamic module results from the net wave-induced depth-integrated fluxes of momentum,

$$S_{xx} = \int_0^{2\pi} \int_0^{\infty} \tilde{E} \left(n \cos^2 \theta + n - \frac{1}{2} \right) \mathrm{d}\sigma \mathrm{d}\theta, \tag{6a}$$

$$S_{xy} = S_{yx} = \int_0^{2\pi} \int_0^{\infty} \tilde{E} n \cos\theta \sin\theta \mathrm{d}\sigma \mathrm{d}\theta, \tag{6b}$$

$$S_{yy} = \int_0^{2\pi} \int_0^{\infty} \tilde{E} \left(n \sin^2 \theta + n - \frac{1}{2} \right) \mathrm{d}\sigma \mathrm{d}\theta, \tag{6c}$$

where $\tilde{E}$ is the spectral wave energy density ($\tilde{E} = N/\sigma$) and

$$n = \frac{|\vec{c}_g|}{c_w} = \frac{1}{2} \left(1 + \frac{2\kappa h}{\sinh 2\kappa h} \right), \tag{7}$$

with $c_w = \sigma/\kappa$ the phase velocity of the waves. Additionally, the wave module provides local data of the significant wave height H_s, peak period T_p, associated wave number κ_p, and peak wave propagation direction θ_p to the hydrodynamic and sediment transport modules.

On the northern boundary, a JONSWAP wave spectrum is prescribed, with a directional spreading with a cosine power of 4 and a peak enhancement factor of 3.3. The prescribed H_s, θ_p, and T_p of the spectrum are varied among different model runs.

2.1.4. Sediment Transport

The sediment transport is calculated following the equations of *van Rijn* [2007a, 2007b]. Both bed load and suspended load transport are considered. Suspended sediment transport is calculated with a depth-averaged advection-diffusion equation,

$$\frac{\partial(hc)}{\partial t} + \frac{\partial(huc)}{\partial x} + \frac{\partial(hvc)}{\partial y} + -\frac{\partial}{\partial x}(hD_H \frac{\partial c}{\partial x}) - \frac{\partial}{\partial y} \left(hD_H \frac{\partial c}{\partial y} \right) = \frac{w_s(c_{eq} - c)}{T_{sd}}, \tag{8}$$

with c the depth- and wave-averaged sediment concentration, D_H the horizontal eddy diffusion coefficient, w_s the settling velocity of the sediment, and T_{sd} a parameter that depends on the frictional and settling velocity. Variable c_{eq} is the equilibrium concentration and is computed based on the assumption that the wave-averaged velocity has a logarithmic profile in the vertical and a reference concentration close to the bottom that incorporates the effect of bed slopes on the threshold of motion (see *van Rijn* [2007b] for details). The right-hand side of equation (8) represents the net exchange of sediment between the water column and the bed. The deposition rate depends on suspended sediment concentration c. The erosion is described by the equilibrium concentration, c_{eq}, and depends on the skin friction exerted by the currents and waves on the grains. The contribution of the waves to this skin friction is quadratic in the near-bed wave orbital velocity,

$$u_{wb} = \left(\frac{1}{2} u_{on}^3 + \frac{1}{2} u_{off}^3 \right)^{1/3}, \tag{9}$$

Here u_{on} and u_{off} are the absolute of the maximum and minimum of the (asymmetric) intrawave near-bed horizontal velocity vector $\vec{u}_{w,t}$, respectively. This velocity vector has the same direction as the waves. In the default setting of the model, $\vec{u}_{w,t}$ is parameterized following *Isobe and Horikawa* [1982] and as modified by *van Rijn et al.* [2004] (the explicit expressions are given on page A-3 of this report). In the discussion section of this study, also the new analytical parameterization of *Abreu et al.* [2010] is considered. In that case the intrawave near-bed horizontal velocity vector reads

$$\vec{u}_{w,t} = u_{rms} f_r \left(\frac{\sin(\omega t) + \frac{r \sin(\phi)}{1+f_r}}{1 - r\cos(\omega t + \phi)} \right) \frac{\vec{c}_w}{|\vec{c}_w|}, \tag{10}$$

where u_{rms} is the amplitude of the symmetric near-bed wave orbital velocity that follows from linear wave theory, $\vec{c}_w/|\vec{c}_w|$ indicates the propagation direction of the wave phase, t is the time, $f_r = \sqrt{1-r^2}$, $\omega = 2\pi/T_p$, r is a nonlinearity measure, and ϕ a phase. *Ruessink et al.* [2012] related both r and ϕ parametrically to the local Ursel number, $Ur = \frac{3}{8}\frac{H_s\kappa_p}{(\kappa_p h)^3}$, which allows for a straightforward implementation of equation (10) into a numerical model.

The bed load transport vector, $\vec{q}_b$, is computed from the wave-averaged bed load transport vector, $\vec{q}_{bw}$, combined with a vector that accounts for the sediment transport by undertow, $\vec{q}_{bu}$. The correction for local bed slope effects is computed following *Bagnold* [1966] and *Ikeda* [1982] and controlled by the parameters α_{BN} and α_{BS} (see *van der Wegen and Roelvink* [2008] for details).

Here $\vec{q}_{bw}$ is computed following *van Rijn* [2007a], i.e., by computing the average of the intrawave bed load transport. Consequently, it is a function of the total intrawave near-bed velocity vector, thus of both $\vec{u}$ and $\vec{u}_{w,t}$.

Bed load transport due to the undertow is accounted for by

$$\vec{q}_{bu} = -\alpha_{UT} c_{eq} \vec{u}_S. \tag{11}$$

In this expression, c_{eq} is the equilibrium concentration that is also used in the advection-diffusion equation for suspended sediment, and α_{UT} is a coefficient that controls the magnitude of the sediment transport due to the undertow. Finally, $\vec{u}_S$ is the Stokes velocity vector due to the presence of waves,

$$\vec{u}_S = \frac{E}{h\rho c_w}\frac{\vec{c}_w}{|\vec{c}_w|}, \tag{12}$$

with E the total wave energy density. The applied parameterization of the sediment transport due to undertow is based upon the fact that in the Delft3D model, suspended sediment is transported with generalized Lagrangian mean velocities, which includes the Stokes velocity by waves. Here $\vec{q}_{bu}$ compensates for this by transporting sediment in the opposing direction. This method resembles the method applied in other studies [e.g., *Reniers et al.*, 2004; *Grunnet et al.*, 2004] and models (XBeach [*Roelvink et al.*, 2009] and Unibest-TC [*Walstra et al.*, 2012]) that parameterize the sediment transport due to undertow by using Eulerian velocities.

In the nearshore zone, $\vec{q}_{bu}$ is directed offshore and $\vec{q}_{bw}$ is generally directed onshore due to the asymmetric wave orbital velocity; consequently, the relative importance of these vectors has a large impact on the development of the beach profile.

The change of the bed level, z_b, is determined at every time step by

$$\frac{\partial z_b}{\partial t} = -\frac{1}{1-p}\left(\frac{\partial q_{b,x}}{\partial x} + \frac{\partial q_{b,y}}{\partial y} + \frac{w_s(c_{eq}-c)}{T_{sd}}\right). \tag{13}$$

Here p is the porosity of the bed.

At the open boundaries of the domain, a zero-concentration gradient is prescribed for the suspended sediment, and z_b at the open boundaries is fixed in time.

2.2. Numerical Aspects

The morphodynamic module is solved on a rectilinear, staggered grid. The grid has a resolution of 1/50 m^{-1} in the region of interest (indicated by the magenta lines in Figure 2a). This region extends 5 km to both the left side and the right side of the inlet and 4.6 km seaward of the inlet. The resolution of the grid that covers the sea outside the region of interest is 1/450 m^{-1}, and the resolution of the grid in the back-barrier basin is 1/150 m^{-1}. To allow for parallel computations, the grid is divided into eight different subdomains using the method of domain decomposition, which is a standard option in Delft3D. In a control run, the resolution of the grid in the back-barrier basin was set to 1/50 m^{-1}; this did not cause qualitative differences in the evolution of the ebb-tidal delta. The time integration is done with an alternating direction implicit scheme (time step of 15 s), and for the spatial discretization a cyclic method is applied [*Stelling and Leendertse*, 1992]. Due to (tidal) variations of the water level, dry cells will be present among the computational cells of the model domain. A simple scheme for the erosion of these dry cells is used; i.e., half of the sediment that is eroded from a wet computational cell located adjacent to a dry cell is supplemented from the dry cell. To reduce computational time, the computed bed level change in equation (13) is multiplied with a morphological acceleration

Table 1. Overview of Conducted Model Runs

Run	Wave Height H_s (m)	Wave Period T_p (s)	Tidal Amplitude A (m)	Breach/No Breach	Initial Bathymetry
1	1.20	5.75	1	No breach	Figure 3a
2	1.20	5.75	1	Breach (600 m)	Figure 4a
3	1.20	5.75	1	Breach (600 m)	Figure 4b
4	1.20	5.75	1	Breach (300 m)	Figure 4c
5	1.20	5.75	1	Breach (300 m)	Figure 4d
6	1.20	5.75	1	Breach (600 m)	Figure 4e
7	1.20	5.75	1	Breach (600 m)	Figure 4f
8	seasonal	seasonal	1	No breach	Figure 3a
9	seasonal + storms	seasonal + storms	1	No breach	Figure 3a
10	0.75	5.34	1	New delta → breach	Figure 2a
11	1.75	6.59	1	New delta → breach	Figure 2a
12	1.20	5.75	0.75	New delta → breach	Figure 2a
13	1.20	5.75	1.5	New delta → breach	Figure 2a
14	1.20	5.75	1	New delta → breach	Small basin

factor, M_{fac} [*Lesser et al.*, 2004; *Roelvink*, 2006], before the bed level is updated. The default value of M_{fac} in this study is 20.

The wave module consists of three nested grids (Figure 2b). The finest grid has a resolution of 1/50 m^{-1} in the region of interest. The intermediate grid has a resolution of 1/450 m^{-1} (size: 40.5 km by 19.5 km). The coarsest grid has a resolution of 1/1350 m^{-1} (size: 135 km by 16.2 km). The directional space covers a full circle and is divided into 36 bins. The frequency space is divided into 24 frequency bins between 0.05 s^{-1} and 1 s^{-1}. Finally, the coupling interval between the morphodynamic module and wave module is 1 h. When the wave module is called, it uses the actual bed level, water level, and flow velocity of the current and sediment transport module. After solving the wave action balance over the domain, it provides the wave conditions that are used in the current and sediment transport module until SWAN is again called.

2.3. Model Simulations

To test the hypothesis that shoals grow as transient features on an ebb-tidal delta when the bathymetry is locally out of equilibrium with the hydrodynamic conditions, multiple runs were evaluated (runs 1 to 9, Table 1). Runs 1, 8, and 9, start with the bathymetry that is shown in Figure 3a. This bathymetry was obtained by running the model for 5 years starting from a no-delta bathymetry (as shown in Figure 2) with the default parameter settings as given in Table 2. Both wave height H_s and wave period T_p at the offshore boundary in the default setup are based upon the average conditions observed at the wave buoy. Furthermore, the wave propagation direction θ_p at this boundary is chosen such that the longshore sediment transport is of the same order as that along the East Frisian Wadden islands [*Ridderinkhof et al.*, 2016]. Run 1 is a continuation of this default run.

Runs 2 to 7 start with an ebb-tidal delta that was as that at the start of run 1, but it was manually breached by extending the main ebb channel and displacing the thereby removed sand to the part of the ebb-tidal delta that is located downdrift of this channel (Figure 4). In this way a local imbalance between the morphology and the hydrodynamic conditions was created. To do this, the ebb-tidal delta was defined as the part of the domain where z_b is more than 0.1 m above the bed level of Figure 2 (no delta) and its local height was defined relative to this no-delta bathymetry. Various bathymetric perturbations were considered. In run 2, the extended channel is 600 m wide, and displaced sand was distributed proportionally to the local height of the downdrift ebb-tidal delta (i.e., locations on the ebb-tidal delta that are higher receive more sand, Figure 4a). In run 3, the channel is 600 m wide, and displaced sand was distributed equally over the downdrift ebb-tidal delta (Figure 4b). In run 4, the channel is 300 m wide and displaced sand was again distributed proportionally to the local height of the ebb-tidal delta (Figure 4c). In run 5, the channel is 300 m wide and sand was distributed proportionally to the local height of the ebb-tidal delta to the power $\hat{n}$, chosen such that the minimum water depth of the downdrift ebb-tidal delta is equal to that of run 2 (Figure 4d). In run 6, the channel

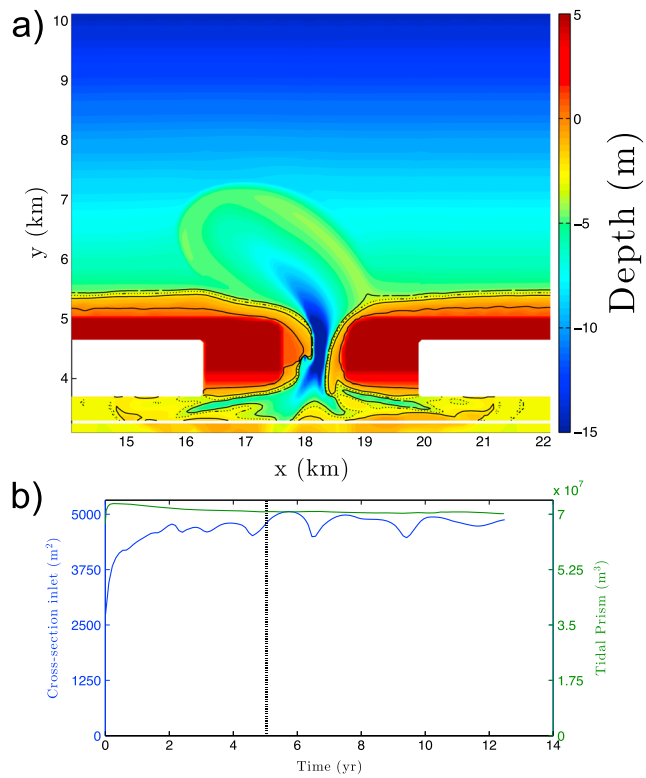

Figure 3. (a) Bathymetry obtained by evaluating the morphodynamic model for 5 years and using default parameter settings. (b) Evolution of tidal prism and cross-sectional area of the inlet shown in Figure 3a. Note that the evolution of the tidal prism and cross-sectional area after 5 years is obtained from *run 1*.

is 600 m wide and the water depth of the entire downdrift ebb-tidal delta was set to the minimum value in run 2 (Figure 4e). In run 7, the channel is 600 m wide and the water depth of the entire downdrift ebb-tidal delta was set to the minimum in run 4 (Figure 4f). Runs 6 and 7 were conducted to assess whether the minimum water depth over the ebb-tidal delta or the volume of the perturbation controls the shoal growth. Note that the sand volume was not conserved by the construction of the initial bathymetries for runs 6 and 7. Also,

Table 2. Default Parameter Settings

Parameter	Value
H_s	1.20 m
D_{50}	250 μm
T_p	5.75 s
ν_e	10 $m^2 s^{-1}$
θ_p	335°
D_H	1 $m^2\ s^{-1}$
A	1 m
M_{fac}	20
ω_{M2}	$1.45 \cdot 10^{-4}\ s^{-1}$
α_{BN}	1.5
f	$1.12 \cdot 10^{-4}\ s^{-1}$
α_{UT}	1.0
ρ	1000 kg m^{-3}
α_{BS}	1.0
p	0.4

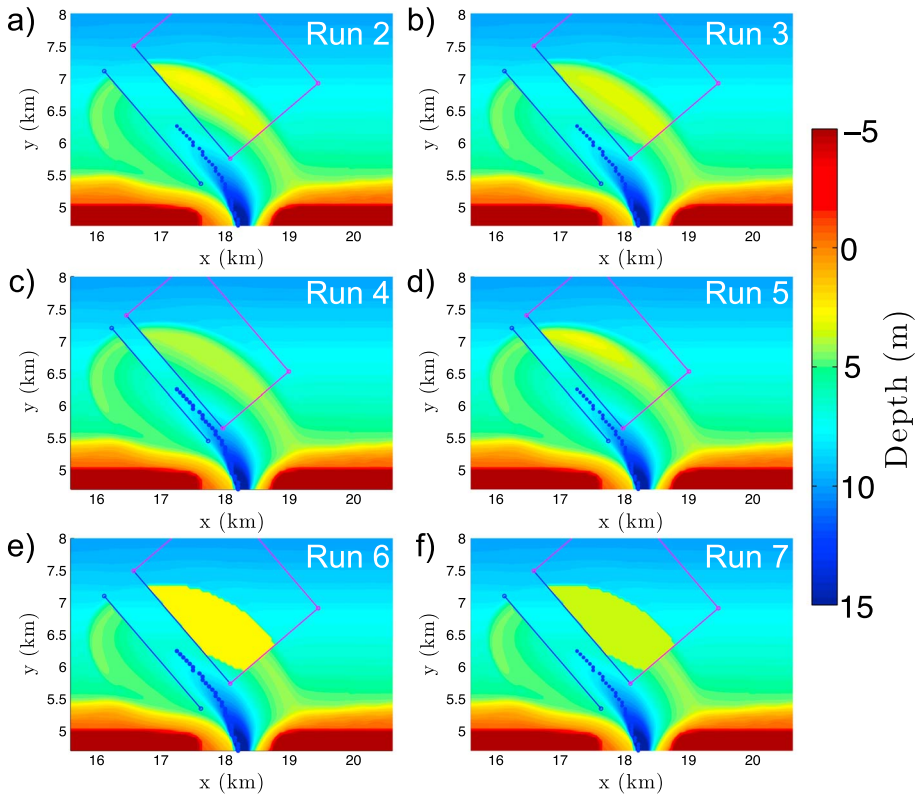

Figure 4. Bathymetries obtained by the imposed breaching of the ebb-tidal delta that is shown in Figure 3a. The blue and magenta lines indicate the borders of the regions in which sand is displaced. The blue dots track the deepest location of the original channel. For details on the design of the breaches, see text. (a) Run 2, (b) run 3, (c) run 4, (d) run 5, (e) run 6, and (f) run 7.

note that the applied perturbations had a negligible effect on the tidal prism (about 1%). To provide details of the model settings, all input files of run 2 have been added as supporting information to this article.

Runs 8 and 9 were executed to assess whether a time-varying wave forcing leads to the formation of migrating shoals on ebb-tidal deltas. In run 8 the model was forced by a seasonal wave climate that was constructed using monthly averaged values of H_s and T_p at the offshore boundary that were based on monthly averages of buoy data. In run 9, the same seasonal wave climate was used, but now six storms with a H_s at the offshore boundary of 3.5 m and three storms with a H_s of 4.5 m (each lasting 1.5 days) were added to the seasonal cycle. This was based upon the occurrence of such conditions at the wave buoy north of Schiermonnikoog. Note that θ_p was constant in these runs and that M_{fac} was set to 1 during the storms.

To evaluate whether shoal migration speed depends on tidal prism and/or average wave height, runs 10 to 14 were executed. In these runs, first an ebb-tidal delta that matches the forcing conditions was allowed to develop by running the model for 5 years, starting from a no-delta bathymetry (Figure 2). Subsequently, this ebb-tidal delta was breached following the same procedure as in run 2, and the development of the shoals on the perturbed bathymetry was evaluated. The migration speed of the shoal was determined as the average speed between 200 days after the imposed breach and the moment that a shoal reaches the coast, where the position of the shoal was defined as the local minimum depth above the shoal.

3. Results

First, the results of the runs in which a breach of the ebb-tidal delta was imposed are presented. Here an analysis of the tidally averaged sediment transport is included to identify the mechanisms that control the growth and migration of the shoals. Tidally averaged transport is considered because it provides insight into the evolution of shoals, which occurs on a time scale that is much larger than a tidal period. Next, the runs with a time-varying wave height are discussed. Finally, the runs in which the tidal range and wave height were varied are presented.

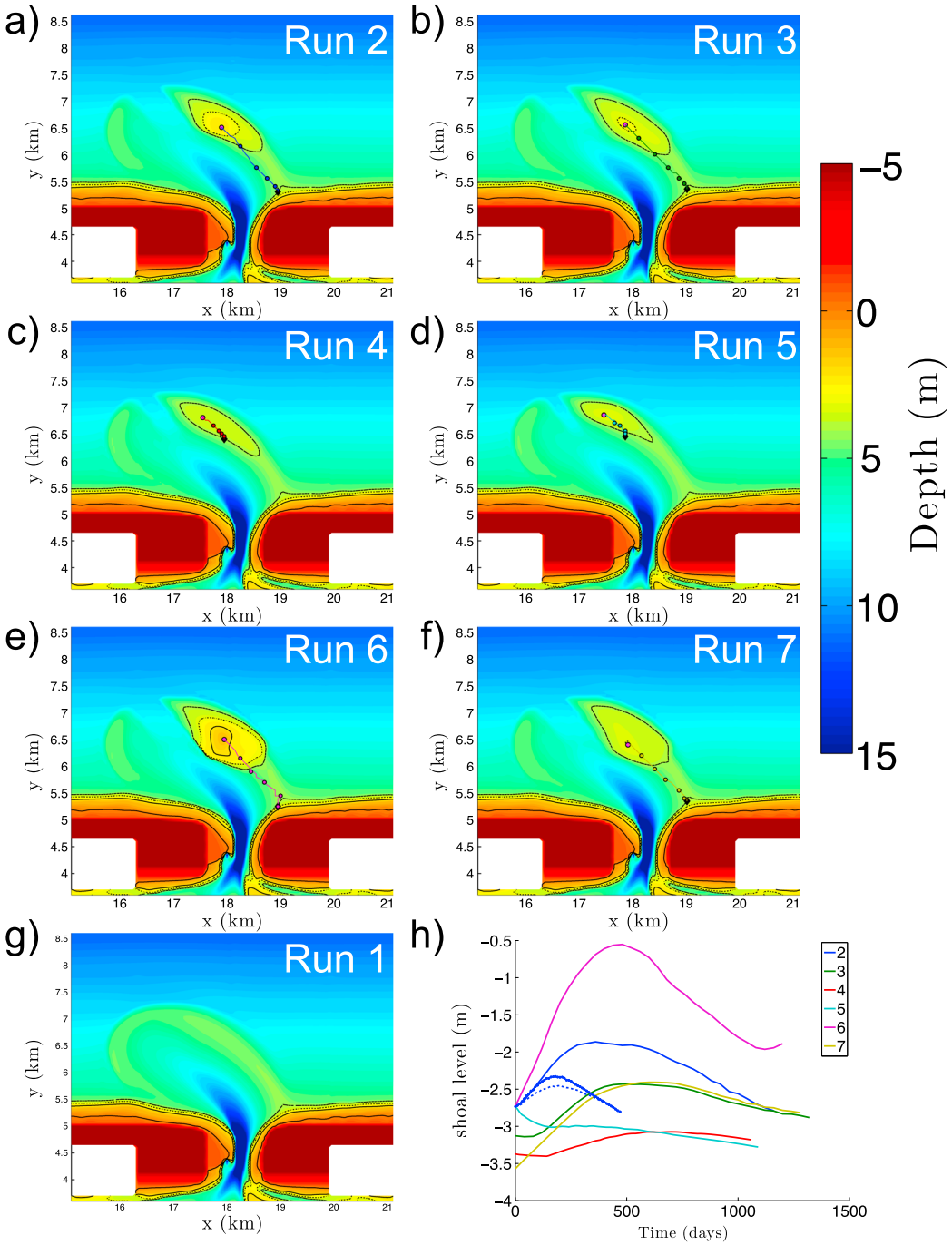

Figure 5. Bathymetry after 200 days of simulation of (a) run 2, (b) run 3, (c) run 4, (d) run 5, (e) run 6, (f) run 7, and (g) run 1. The magenta dot indicates the location of maximum shoal level (minimum water depth) that formed in runs 2 to 7. The colored lines indicate the path that this maximum shoal level follows until it reaches its most landward location (black diamond). The additional dots indicate the position of the shoal every 200 days. (h) The time evolution of the maximum shoal level (relative to mean sea level) in the different runs is displayed. Here the blue dashed (dotted) line indicates the evolution of the shoal that formed in run 2 without asymmetric waves (and undertow). Note that these latter shoals did not reach the downdrift coast.

3.1. Imposed Breach Experiments

3.1.1. Morphodynamic Simulations

In all simulations in which the ebb-tidal delta was breached with a 600 m wide channel (runs 2, 3, 6, and 7), a shoal formed on the perturbed ebb-tidal delta (Figures 5a, 5b, 5e, and 5f). These shoals increased in height during the first part of the simulation; i.e., the minimum water depth above these shoals decreased after the initial perturbation. This is visible in Figure 5h, which shows the time evolution of the maximum shoal level relative to the mean sea level. Furthermore, all shoals that formed in runs 2, 3, 6, and 7 migrated toward the downdrift coast. On the contrary, in the simulations in which the ebb-tidal delta was breached with a channel that has a width of only 300 m (runs 4 and 5), no shoals migrated to the downdrift coast. A shoal did form in run 4, but it disintegrated on the ebb-tidal delta (Figure 5c), and both its growth rate and the maximum height it reached were smaller than those of the shoals that formed in runs 2, 3, 6, and 7 (Figure 5h). In run 5 the minimum depth only increased in time after the initial perturbation; thus, no shoal formed. In the simulation in which the bathymetry was not perturbed (run 1, Figure 5g), no shoal formed on the ebb-tidal delta.

The fact that in runs 1, 4, and 5 no shoal migrated to the downdrift coast suggests that a necessary condition for such shoal migration in the employed setup is that the perturbation must exceed certain thresholds, which are likely related to minimum water depth and sand volume. However, note that the initial water depth above the perturbation in run 4 equals that in run 7, and in the latter simulation a shoal formed and migrated to the downdrift coast, so this threshold is not controlled only by the minimum water depth of the initial perturbation. The amount of sand that is displaced in runs 4 and 5 is smaller than that in all other of these runs ($\sim$34% of that in run 7 and $\sim$48% of that in runs 2 and 3). Apparently, the volume of sand displaced must exceed a critical value in order to form a shoal that migrates to the downdrift coast. Interestingly, despite the fact that there was more sand displaced in run 7 than in run 2, the different distributions caused the shoal in run 2 to grow higher and migrate faster than the shoal in run 7. Thus, the development of the shoal is affected by both the volume and the distribution of this volume in the initial perturbation. The fact that the shoal in run 6 became the highest of all shoals in different runs shows that not only shape matters but also size. The flat shape of the dumped sand in runs 6 and 7 is still outstanding compared to its surroundings and therefore substantially affects the waves and tidal currents. Also the depth of the perturbation determines the degree by which it influences waves and currents.

3.1.2. Mechanism of Shoal Growth

To investigate why a shoal only formed on perturbed bathymetries, in Figure 6 the amplitude of near-bed wave orbital velocity (u_{rms}), wave energy flux ($\vec{c}_g E$), and tidally averaged residual currents at the beginning of run 1 and 2 are shown. Moreover, in Figures 6c and 6d, the wave-induced residual currents at the beginning of run 1 and 2 are displayed. These were constructed by subtracting the tidally averaged residual currents of a tides-only simulation from the residual currents due to both waves and tides. Figures 6a and 6b reveal that u_{rms} is much larger on the perturbed (shallower) ebb-tidal delta. This is a result of the decreased water depth, which causes wave shoaling and the focusing of wave energy over the shallower bathymetry. A comparison between the magnitude of the maximum and mean instantaneous tidal currents and the maximum and mean u_{rms} revealed that skin friction on the ebb-tidal delta is predominantly caused by wave orbital motion (not shown). Note that this is not the case in the channel that intersects the ebb-tidal delta. Consequently, a higher u_{rms} strongly increases the skin friction on the shoal, which increases the stirring of sediment and leads to strong erosion and a high sediment concentration.

The wave-driven residual currents are also much larger over the perturbed ebb-tidal delta than over the undisturbed delta. This is a result from the increased wave energy dissipation over the shallow bathymetry, which increases the wave-induced forces. The wave-driven residual currents are the main contributors to the total tidally averaged residual currents (Figure 6) and cause the residual currents over the shallow part of the perturbed ebb-tidal delta to be directed landward and alongshore. In contrast, the residual currents over the unperturbed delta are directed seaward.

Ultimately, the joint action of (1) the increased wave-driven residual currents and (2) the increased skin friction leads to a residual sediment transport pattern that causes the growth of a shoal on the perturbed bathymetry (Figure 7). The tidally averaged sediment transport shows strong convergence/divergence patterns on the entire perturbed ebb-tidal delta. In run 1 (unperturbed bathymetry), the sediment transport over the ebb-tidal delta is much smaller and only converges at the seaward edges of the ebb-tidal delta. The latter is responsible for the (slow) expansion of the ebb-tidal delta during this simulation.

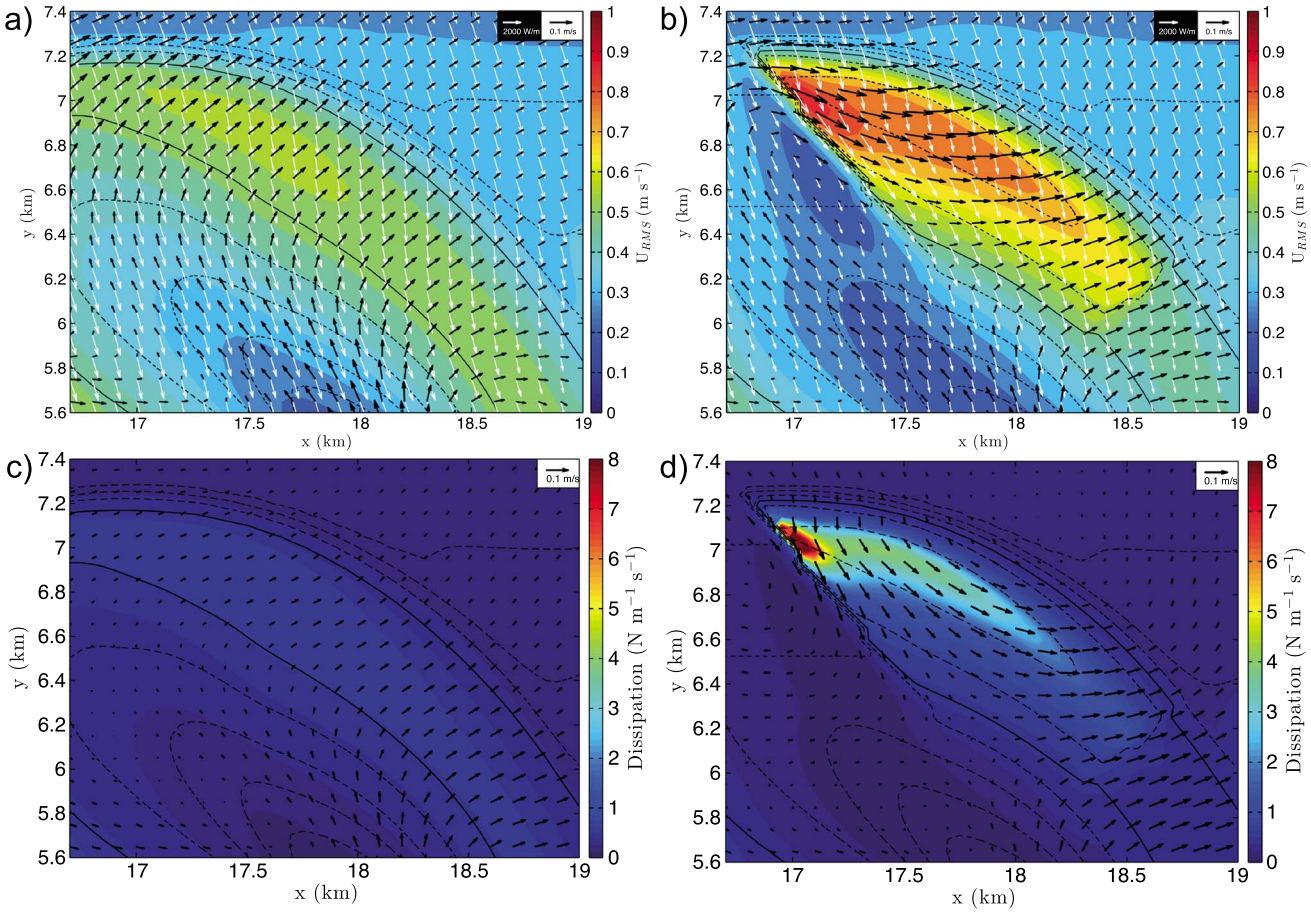

Figure 6. (a and b) The amplitude of the near-bed wave orbital velocity (colored contours), wave energy flux (white arrows), and tidally averaged residual currents (black arrows) in the area of the shoal, at the start of (Figure 6a) run 1 and (Figure 6b) run 2. (c and d) The wave-driven residual currents (black arrows) and the wave energy dissipation (colored contours) at the start of (Figure 6c) run 1 (Figure 6d) run 2. The black contour lines indicate the depth in all panels.

3.1.3. Mechanism of Shoal Migration

To identify and assess the mechanisms that cause the migration of shoals, the tidally averaged sediment transport over the bathymetry that was obtained after 200 days in run 2 was investigated (Figure 8). The sediment transport patterns in the standard setting, i.e., transport due to tides and waves with an asymmetrical orbital velocity (Figure 8a), without tides (Figure 8b), without waves (Figure 8c), and with a symmetrical wave orbital velocity (Figure 8d) are considered. In the standard setting, divergence of sediment transport occurs in the region seaward of the highest part of the shoal (tilted toward the direction of wave incidence), and convergence of sediment transport is found on the landward side of this local maximum, which causes the shoreward migration of the shoal. This sediment transport pattern is more pronounced when tides are not considered (Figure 8b) and absent when waves are not considered (Figure 8c), thereby indicating that waves are primarily responsible for this pattern.

Sediment transport due to asymmetric waves contributes to the growth and migration of shoals, as it causes sediment transport in the direction of wave propagation and the latter converges toward the shoal because of depth-induced refraction. Interestingly, when the effect of asymmetric waves is omitted, the initial development of the shoal is barely affected (Figure 5h), implying that the effect of asymmetric waves is not a crucial factor for shoal growth. The main difference in the sediment transport patterns with and without asymmetric waves (Figures 8a and 8d) is that in the latter case, a second region of sediment convergence is prominent on the edge of the ebb-tidal delta. This implies that sediment transport due to asymmetric waves adds to maintaining the shoal as a coherent feature. This was confirmed by repeating run 2 with a symmetric wave orbital velocity. In that case a similar shoal as in run 2 formed, but its growth ceased, and it disintegrated before reaching the downdrift coast (results not shown).

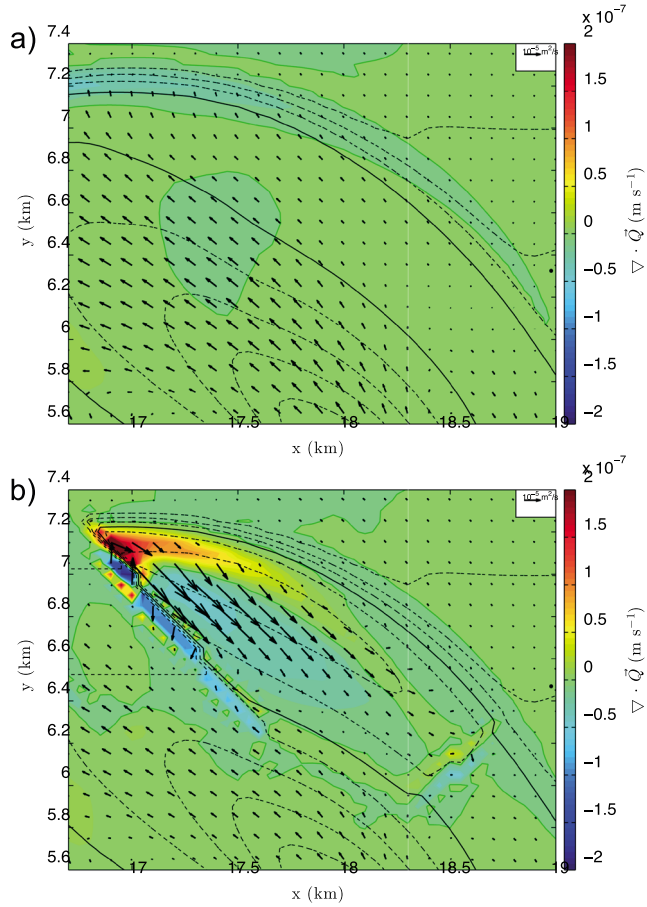

Figure 7. The tidally averaged sediment transport (black arrows) and its divergence $\nabla \cdot \vec{Q}$ (colored contours) in the area of the shoal, at the start of (a) run 1 (unperturbed bathymetry) and (b) run 2 (perturbed bathymetry). Positive (negative) contours indicate erosion (sedimentation). The black contour lines indicate the local water depth (thick line: $h = -5$ m; dashed lines: every 1 m). Vectors are drawn every fourth grid point.

The shoal migrates toward the coast because the tidally averaged sediment transport increases toward the location where the water depth above the shoal is minimal and converges landward of this location. Convergence/divergence patterns of sediment transport are mainly controlled by the gradient of the total depth-averaged sediment concentration $\bar{c}$ (including bed load transport and proportional to skin friction over water depth) in the direction of the residual currents [*Ribas et al.*, 2015]. Since wave energy density focusses toward the local minimum water depth and u_{rms} increases with decreasing water depth, $\bar{c}$ is maximum at the shallowest part of the shoal, while the gradients in $\bar{c}$ are the largest on the edges of the shoal. Moreover, the residual currents are directed landward over the shoal (see, e.g., Figures 6 and 9); these currents are primarily wave driven and much more prominent when a shallow feature is present on the ebb-tidal delta because the driving force of wave-driven currents is closely related to the wave energy dissipation [*Dingemans et al.*, 1987].

3.2. Time-Varying Wave Height

Forcing the model with a monthly averaged H_s (run 8) leads to results that are similar to those when the model was forced with a constant H_s (run 1). A persistent local minimum in the water depth is found ~1000 days after the start of run 8 (Figure 10a), but this does not develop into a migrating shoal during the model run.

Adding 12 stormy days to the seasonal cycle (run 9) has major implications for the development of the bathymetry during the simulation (Figures 10c and 10d). A shoal develops, which migrates some distance landward (510 m between the time slices shown in Figures 10c and 10d). However, during the evaluated time the shoal does not reach the downdrift coast (i.e., after 2700 days). Interestingly, this shoal only gained in height during storms and lost height during calm weather conditions (Figure 10e). The local imbalance between the bathymetry and wave conditions during storms thus results in the formation of shoals on the ebb-tidal delta according to the mechanisms that were described in sections 3.1.2 and 3.1.3.

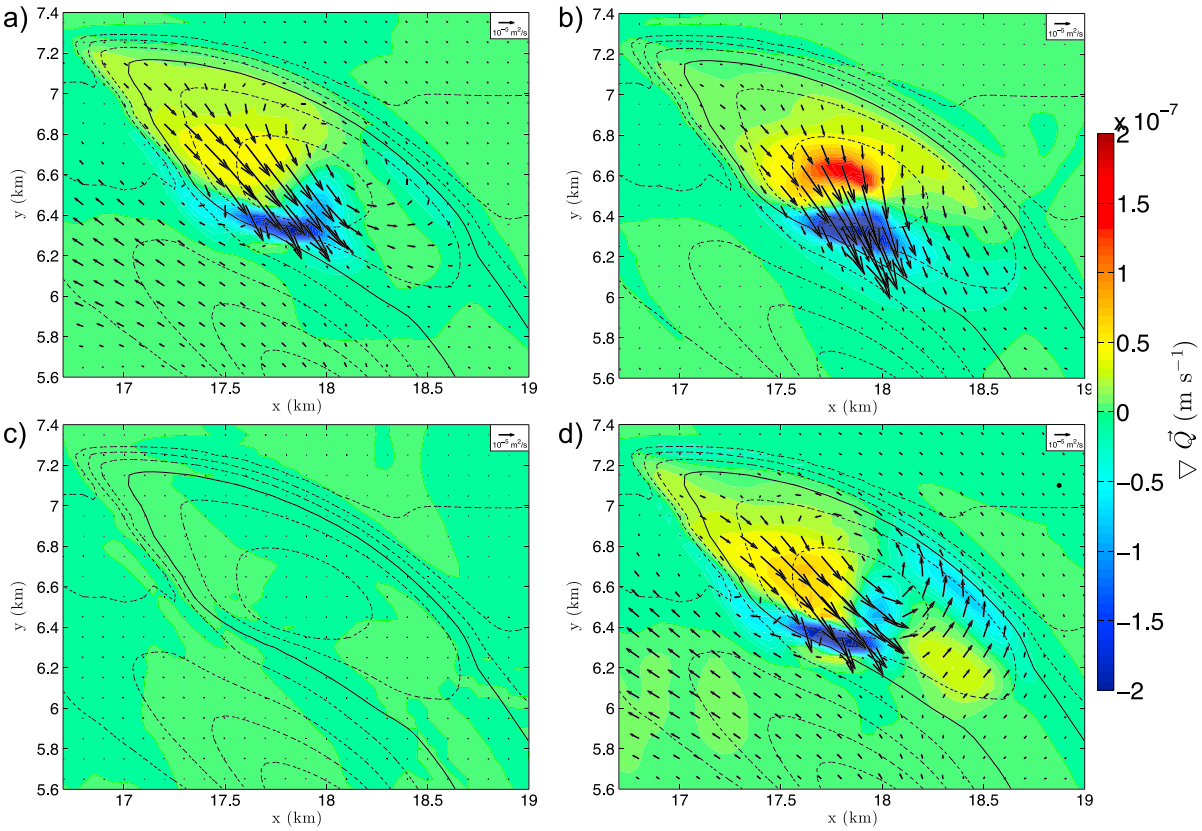

Figure 8. The tidally averaged sediment transport (black arrows) and its divergence $\nabla \cdot \vec{Q}$ (colored contours) in the area of the shoal that is obtained in run 2 after 200 days. Positive (negative) contours indicate erosion (sedimentation). The black contour lines indicate the local water depth (thick line: $h = -5$ m). (a) All processes included. (b) No tidal forcing. (c) No wave forcing. (d) Symmetric wave orbital velocity. Vectors are drawn every fourth grid point.

3.3. Dependence of Shoal Migration on Tidal Prism and Wave Height

To evaluate whether the shoal migration speed depends on the tidal prism and/or average wave height, runs 2 and 10–14 were analyzed (Figure 11). In the standard setting (run 2) the shoal migrated with an average speed of 629 m yr^{-1}. Faster migrating shoals were found for higher waves (run 11: 1477 m yr^{-1}) and smaller tidal prism (run 12: 946 m yr^{-1}; run 14: 754 m yr^{-1}), whereas migration speed of shoals is smaller with smaller waves (run 10: 306 m yr^{-1}) or larger tidal prism (run 13: 337 m yr^{-1}). The influence of incident wave energy on migration speed was to be expected as Figure 8 revealed that waves are primarily responsible for the shoal migration. The main reason for the effect of the tidal prism on the migration speed of the shoal is that the tidal prism controls the relative importance of tidal currents compared to wave-driven residual currents to the total tidally averaged residual currents. To illustrate this, the effect of a smaller tidal prism on the hydrodynamics and sediment transport patterns over the bathymetry that was obtained after 200 days in run 2 is shown in Figure 9. Here the tidal prism was reduced from $\sim 7.5 \cdot 10^7$ m^3 to $\sim 5.5 \cdot 10^7$ m^3 by connecting the tidal inlet to a smaller back-barrier basin. In Figure 9a, the resulting residual currents and sediment transport patterns are displayed. Figure 9b shows the difference between the residual currents in the original run 2 (Figure 8a) and those in the run with decreased tidal prism (Figure 9a). Also, differences in sediment transport vectors and divergence/convergence patterns between those runs are shown. A larger tidal prism increases the seaward directed residual currents over the landward part of the shoal, which decreases the convergence of sediment in the propagation direction of the shoal. Thus, the tidally driven residual currents counteract the wave-driven residual currents that are the main cause of the landward migration of the shoals. Therefore, an increase of the strength of the tidally driven residual currents decreases the shoal migration speed, and a decrease of the strength of the tidally driven residual currents increases the shoal migration speed.

Although the tidal prism in runs 12 and 14 was almost equal ($\sim 5.5 \cdot 10^7$ m^3), the morphology of the ebb-tidal deltas in these runs is quite different. This is because the interaction between the cross-shore and alongshore tidal currents affects the orientation of the ebb-tidal delta [*Sha and van den Berg*, 1993; *Ridderinkhof et al.*,

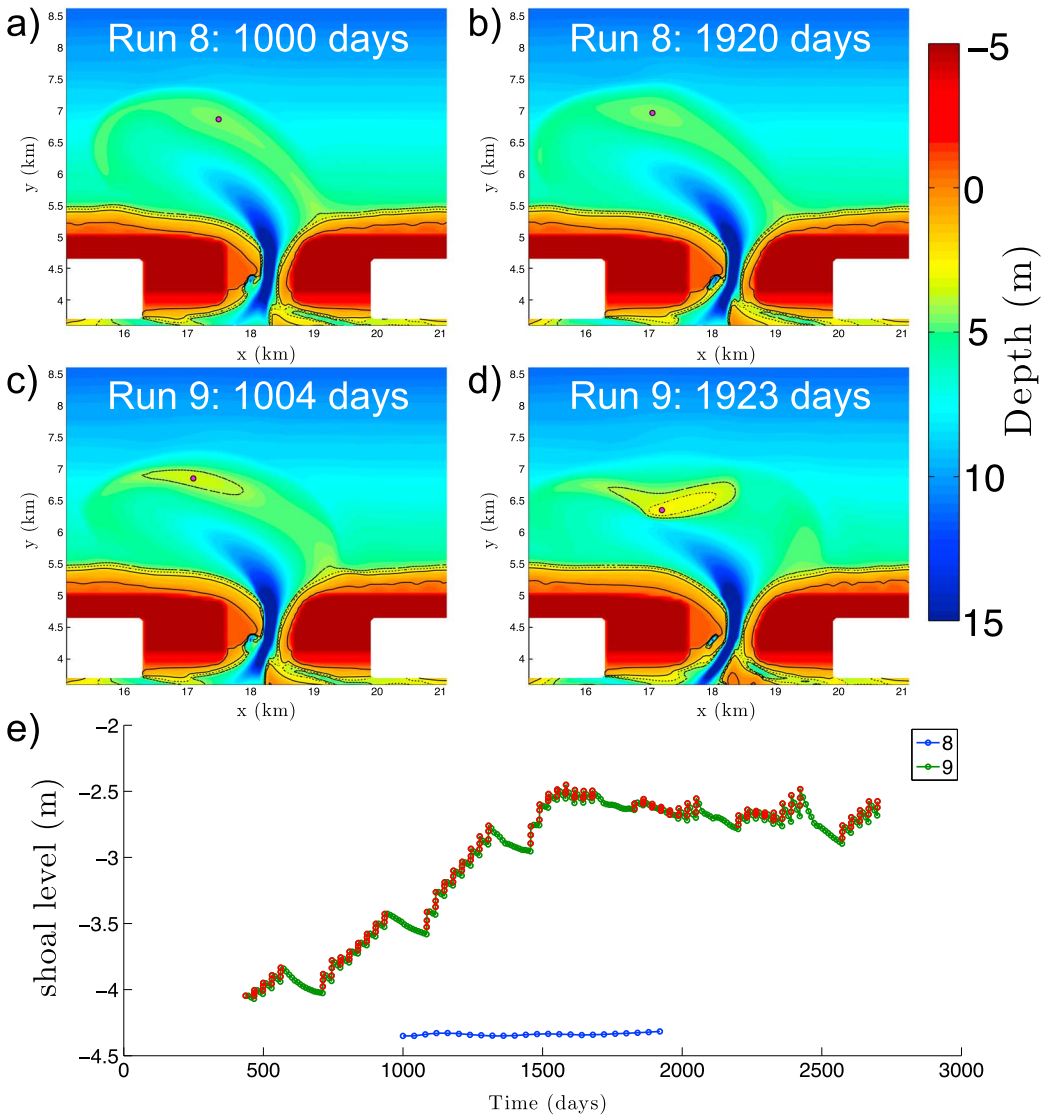

Figure 9. (a) Tidally averaged residual currents (black arrows), sediment transport vectors $\vec{Q}$ (white arrows), and divergence (colored contours) over the shoal that formed after 200 days in run 2. Here the tidal prism is reduced by 25% by decreasing the tidal basin area. (b) Difference between the situation in run 2 after 200 days and a situation with the same bathymetry in which the tidal prism was reduced. Shown is the difference between tidally averaged residual currents (black arrows), sediment transport vectors (white arrows), and divergence of sediment transport (colored contours). In both panels, black contour lines indicate the local water depth.

2014], and the alongshore tidal currents decrease in strength only when the tidal prism is decreased by reducing the tidal range (in that case $\partial\eta/\partial x$ decreases). Note that the imposed perturbation in run 12 raised the downdrift ebb-tidal delta above sea level. Although the maximum height of this perturbation only decreased during this run, it was decided to define the coherent feature that moved to the coast as a shoal. In a control run, in which the bathymetry of run 12 was perturbed by a 300 m wide channel a shoal that increased in height did form, this shoal had a smaller volume and consequently migrated toward the coast with a larger speed (not shown).

4. Discussion

In this study it is shown that shoals both grow and migrate as a result of a local imbalance between the morphology of an ebb-tidal delta and the wave conditions. When waves encounter a relatively shallow feature, dissipation of their energy over this bathymetry causes gradients in radiation stresses that drive residual

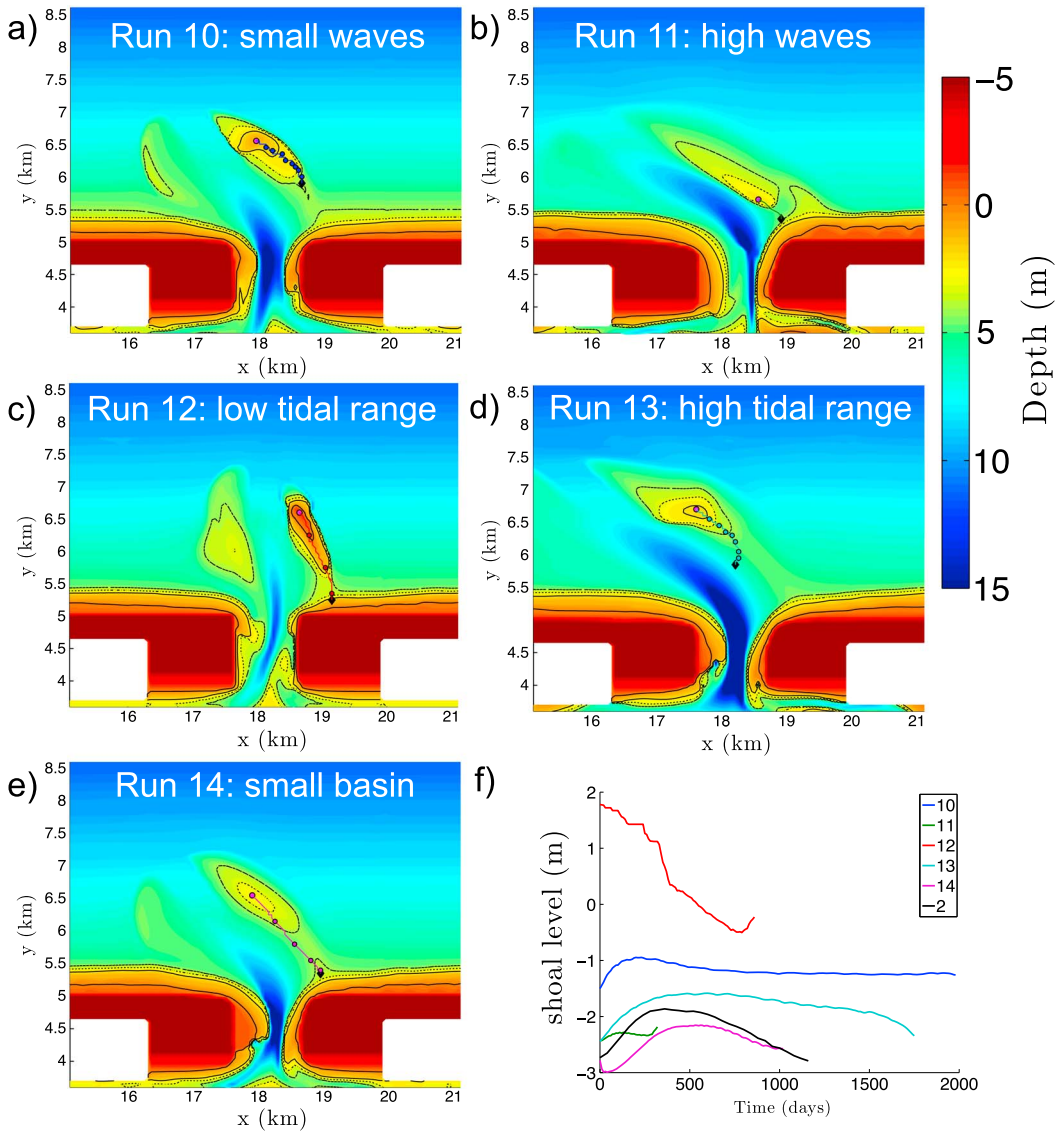

Figure 10. Bathymetry of (a) run 8 after 1000 days, (b) run 8 after 1920 days, (c) run 9 after 1004 days, and (d) run 9 after 1923 days. (e) The time evolution of maximum shoal level (relative to mean sea level) in these runs is displayed. Here the *red circles* indicate moments that the model is forced by storm conditions. In these periods that last 1.5 day each, the shoal height increases.

currents (as was observed by *Bertin et al.* [2009a]) toward the coast over the location of the local minimum water depth (e.g., Figure 9a). Together with increased wave stirring in shallower water these residual currents lead to a convergence of sediment transport on and just landward of shallowest region of the shoal. This mechanism resembles that described by *Ribas et al.* [2015], who explained the growth and migration of other morphological features in the near-shore zone (e.g., crescentic bars) by the presence of currents across gradients in depth-averaged sediment concentration. An important difference between the formation of shoals on ebb-tidal deltas and sandbars closer to the coast is that there is no closed boundary (coastline) immediately beyond the ebb-tidal deltas. Consequently, at ebb-tidal deltas the shore normal wave force cannot be balanced by a pressure gradient force that follows from a setup of water against the coast. Therefore, waves cause landward residual currents over shoals on ebb-tidal deltas; these play a dominant role in the net sediment transport.

The local imbalance that leads to the growth of shoals that form in this study are manifestations of the system to adjust to suddenly changed conditions. These conditions were either caused by adding incidental storms to the wave forcing or by an imposed perturbation of the ebb-tidal delta. The latter were based on natural

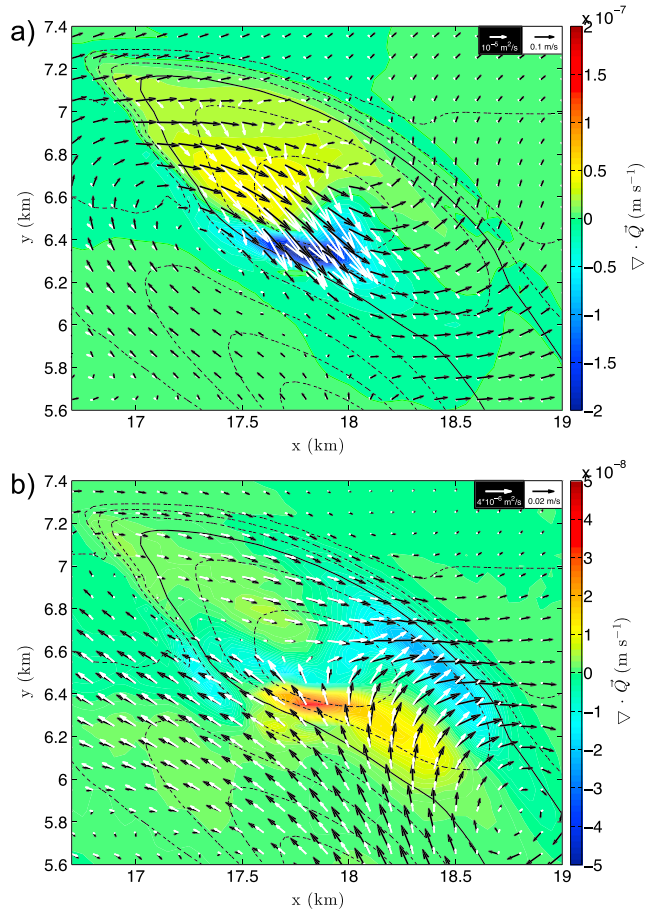

Figure 11. Bathymetry 200 days after the bathymetry was perturbed in runs (a) 10, (b) 11, (c) 12, (d) 13, and (e) 14. The magenta dot indicates the location of the minimum water depth above the shoal. The colored lines indicate the path that the shoal follows until it reaches its most landward location (black diamond). The additional dots indicate the position of the shoal every 200 days. (f) The time evolution of the maximum shoal level (relative to mean sea level) is displayed. Here the black line indicates the evolution of the shoal that formed in run 2.

breaches that occur on the ebb-tidal deltas of the Wadden Sea, such as at Ameland Inlet (Figure 12). This is different from the shoals that developed in the simulations of *Nahon et al.* [2012] and *Dastgheib* [2012], which originated from a continuous imbalance between morphology and wave conditions due to the high energetic wave forcing. For that setting large morphological changes occur in the entire nearshore zone. Furthermore, on many ebb-tidal deltas such conditions only persist during short times (~days). Note that average wave conditions do not necessarily correspond to average sediment transport rates as the sediment transport rate increases nonlinearly with increasing wave height. Similar shoal migration as found by *Nahon et al.* [2012]; *Dastgheib* [2012] occurred in the model set-up of this study in a control run where H_s was set to 3 m (see animation in the supporting information).

The modeled morphodynamic response to storms, i.e., increase of shoal height and landward migration of the shoal, is consistent with the observations of *Hands and Shepsis* [1999] and *O'Connor et al.* [2011]. They detected large-scale morphological changes and shoal migration on different ebb-tidal deltas (Washington, USA, and Ireland) in time periods that were characterized by an increased storminess.

Not all shoals that formed remained coherent features. In the runs where a small sand volume was displaced (runs 4 and 5), convergence of wave-driven sediment transport could not overcome divergence of the sediment transport due to other processes (e.g., bed slope effects and tidal currents) and the shoal disintegrated (Figure 5). It was shown that asymmetric waves add to maintaining the shoal as a coherent structure and that without incorporating this process, the shoal that formed in the standard model setup (run 2) does not reach the coast. The channel also plays an important role in the development of the shoal. This is concluded from an

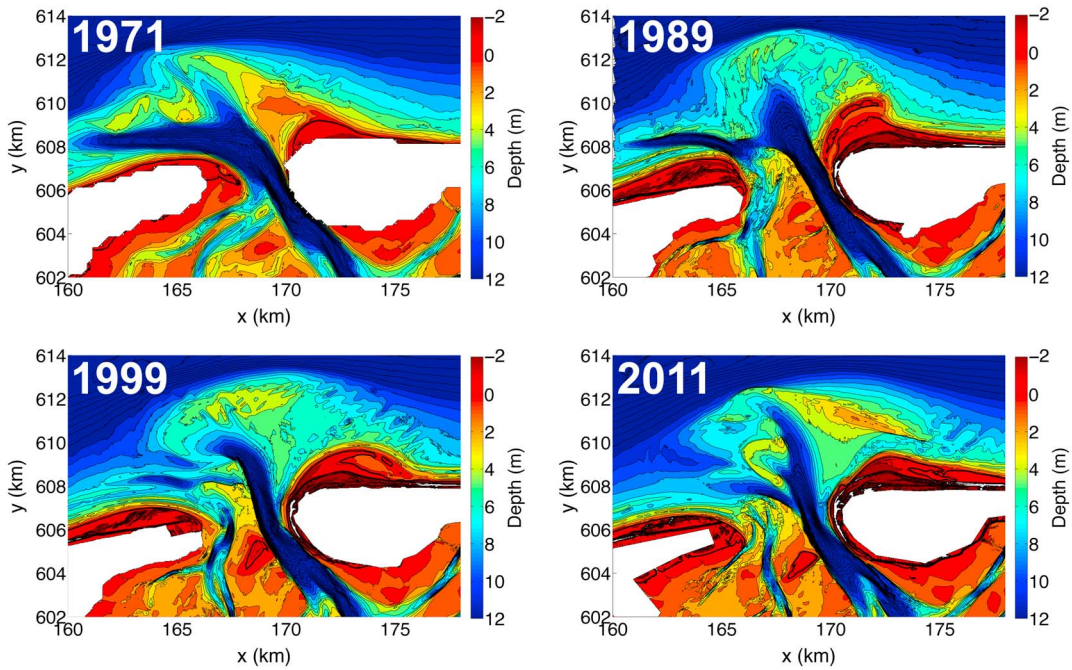

Figure 12. Bathymetries of the ebb-tidal delta of the Ameland Inlet in 1971, 1989, 1999, and 2011. They reveal the presence of migrating shoals; one shoal attached to the coast around 1989 and a succeeding shoal are still seaward of the island Ameland in 2011. The bathymetric measurements were obtained by *Rijkswaterstaat*.

additional run in which the same sand volume and shape as in run 2 was dumped, but the original channel was not extended (see supplementary material). In this simulation, a shoal did develop but migrated slower and did not reach the downdrift coast. This seems to be because without the presence of the extended channel, the tidal currents that oppose the landward sediment transport are more important over the shoal.

Recently, *Abreu et al.* [2010] introduced an alternative parameterization of the asymmetric near-bed wave orbital velocity, $\vec{u}_{w,t}$. To test the robustness of our results, an additional run was executed with this new parameterization for $\vec{u}_{w,t}$, and the rest of the setup equals to that in run 2. Also with the alternative parameterization of $\vec{u}_{w,t}$, a shoal forms and migrates to the downdrift coast (Figure 13). The difference in shoal evolution stems from the higher magnitude of $\vec{u}_{w,t}$ in shallow water in the parameterization of *Abreu et al.* [2010], which leads to higher sediment transport rates. Consequently, the shoal migrates faster, and the initial growth rate as well as the decay rate in a later stage of its evolution are larger.

The migration speed of the shoals increases with a decreasing tidal prism and with increasing incident wave energy. This is because in the model waves are the main driver of the shoal migration. The dependence of shoal migration on incident wave energy was not reported in data analysis studies, probably because it is complicated to distinguish the wave energy effects from other parameters that vary among inlets. The negative relationship between tidal prism and shoal migration speed that was found agrees with what was observed for the shoals that migrate on the ebb-tidal deltas of the Wadden Sea [*Ridderinkhof et al.*, 2016]. Furthermore, the findings are in line with the statement of *FitzGerald* [1982] that the migration speed depends on tidal range, wave energy, and local water depth.

Since this study aimed at identifying the physical processes that lead to the growth and migration of shoals on ebb-tidal deltas and at assessing the relative importance of the wave and tidal forcing on shoal behavior, a highly idealized model setup was chosen. In particular, the wave forcing and the initial bathymetries were highly schematized. Moreover, the effect of wind and of the presence of various grain sizes was not considered. The migration speed of the shoals in the simulations (~600 m yr^{-1}) is larger than that of observed shoals (~300 m yr^{-1}). Moreover, the decrease of the migration speed with increasing tidal prism obtained with the model is a factor four times larger than that is reconstructed from field data of migrating shoals on the ebb-tidal deltas of the Wadden Sea [*Ridderinkhof et al.*, 2016]. Note that the migration speed of the shoal that

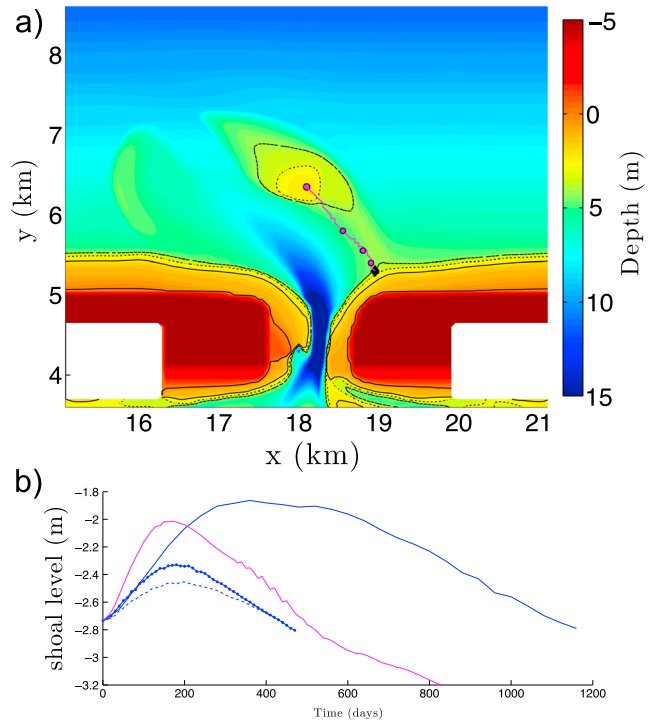

Figure 13. (a) Bathymetry after 200 days of a simulation where the formulation of *Abreu et al.* [2010] is used to describe the near-bed wave orbital velocity vector, $\vec{u}_{w,t}$. The magenta dots indicate the location of the maximum shoal level every 200 days. The colored lines indicate the path that the shoal follows until it reaches its most landward location (black diamond). (b) Time evolution of the maximum shoal level of the shoal that formed when $\vec{u}_{w,t}$ was obtained from *Abreu et al.* [2010] (magenta line), obtained from *Isobe and Horikawa* [1982] (blue solid line), symmetric (blue dashed line), symmetric and undertow was omitted (blue dotted line).

formed in the simulation in which occasional storms were added to the forcing was much lower than that of the shoals that resulted from the imposed breaching of the ebb-tidal delta.

Bruneau et al. [2011] showed that interannual and decadal variability of the wave climate has a large impact on the morphology of the Óbidos inlet system, such variation was not considered in this study. The wave propagation direction at the offshore boundary was constant in time, which is one of the potential reasons for the fast migration of the shoals in the simulations. Furthermore, the prescribed wave period T_p at the offshore boundary was set to the average that was observed for the prescribed wave height. Varying T_p independently alters the wave steepness, a parameter that is known to affect the balance between offshore and onshore sediment transport [*Ranasinghe and Pattiaratchi*, 2003] but is beyond the scope of this study. Moreover, in the model setup the sand was assumed to have a constant grain size. Consequently, grain sorting effects that are observed on ebb-tidal deltas [e.g., *Soo Son et al.*, 2011] and could potentially decrease gradients in the bathymetry were excluded. The effect of infragravity waves on the formation of the shoals was not considered. These are not of primary importance but could possibly alter the development of the morphological features [see also *Reniers et al.*, 2004].

The sediment transport formula that was used belongs the most recent and sophisticated that exists, such that the effect of asymmetric waves, settling lags, threshold of motion, and bed slope effects were incorporated. An additional sediment transport component due to undertow was incorporated to allow for a sediment balance in the cross-shore direction. This was not crucial for simulating the growth and migration of the shoal but allowed for a more realistic evolution of the beach profile. *Bertin et al.* [2009b] and *Dissanayake et al.* [2009] showed that different results are to be expected when other sediment transport formulas are used, but the physical mechanism that is responsible for the growth and migration of shoals will probably not change because the essential processes, i.e., wave energy focusing and generation of wave-driven residual currents, would still occur.

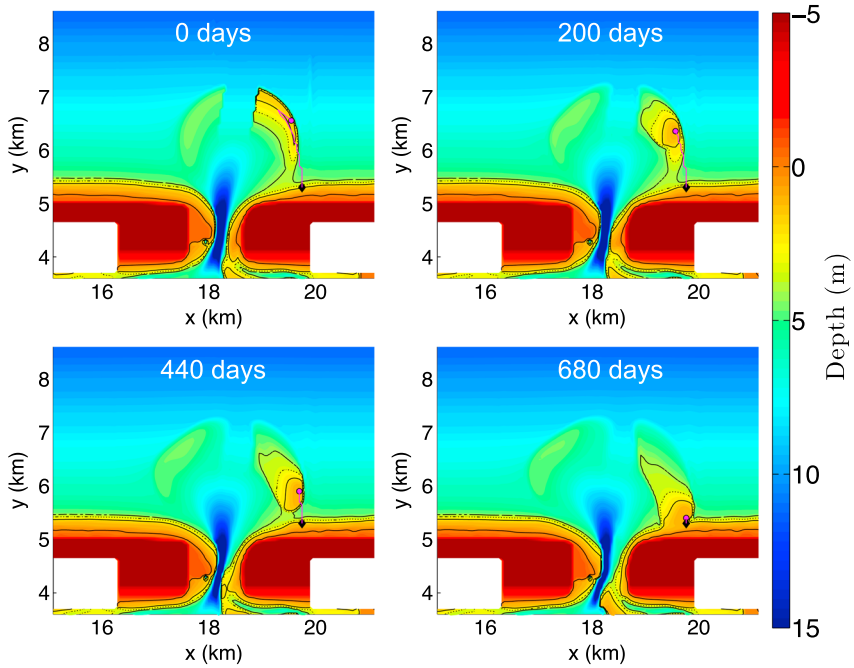

Figure 14. The evolution of a simulation in which the tidal wave has no alongshore phase propagation. Days are counted from the moment that the ebb-tidal delta was manually perturbed. A shoal forms and migrates toward the downdrift coast. The magenta line indicates the path that the maximum shoal level follows until it reaches its most landward location (black diamond).

In all the previously discussed simulations, the imposed tidal forcing is that of an alongshore propagating wave. Due to the joint action of the cross-shore and alongshore tidal currents, the simulated ebb-tidal deltas are oriented updrift (such as observed at many Wadden Sea inlets, *Sha and van den Berg* [1993]). To verify that, the results also hold when the alongshore phase propagation of the tidal wave is negligible, typical for the U.S. East Coast, an additional simulation was performed. Again, first an ebb-tidal delta was developed, which was subsequently manually perturbed. Also, in this simulation a shoal formed and migrated toward the downdrift coast (Figure 14).

5. Conclusions

With the use of a numerical morphodynamic model, ebb-tidal deltas and shoals on these deltas were simulated in an idealized tidal inlet system that was forced by both waves and tides. It was found that shoals on ebb-tidal deltas grow as a result of a local imbalance between wave conditions and the bathymetry. In this study, the imbalance was imposed by redistributing the sand on the ebb-tidal delta or by adding storms to the wave forcing. Shoals grow and migrate due to the convergence of sediment transport on top and landward of the shoal, which is primarily driven by the joint action of gradients in sediment stirring due to variations in water depth and wave-driven residual currents over the shoal. There are thresholds for the local imbalance below which a shoal does not form; these thresholds are related to the minimum water depth, sand volume, and local wave height.

Incidental high energetic wave condition such as present during storms are typically not in balance with the bathymetry of an ebb-tidal delta, which evolves at a much larger time scale. It was found that such storms can generate a shoal on an ebb-tidal delta that persists during normal wave conditions and continues to grow during subsequent storms.

Sediment transport driven by asymmetric near-bed wave orbital velocities contributes to the formation and migration of shoals because it is directed in the direction of wave propagation. Considering asymmetric near-bed wave orbital velocities was a requirement for the shoals to maintain as a coherent feature and reach the downdrift coast in this study. Two different parameterizations of this velocity were implemented, which gave qualitatively similar results.

The migration speed of shoals on ebb-tidal deltas was found to increase with increasing incident wave energy and decreasing tidal prism. Larger waves increase the sediment transport driven by waves and consequently the shoal migration. A larger tidal prism increases the tidally driven residual currents, these counteract the wave-driven residual currents that induce the shoal migration. A smaller tidal prism causes a larger shoal migration speed.

Acknowledgments
The parameter settings used in the model are listed in the tables of this manuscript. Furthermore, all input files of run 2 can be found in the supporting information. We thank *Rijkswaterstaat* for making their bathymetric and wave data available, which can be found at *opendap.deltares.nl*. This research was funded by the Netherlands Organisation for Scientific Research (NWO) (project 821.01.010).

References

Abreu, T., P. A. Silva, F. Sancho, and A. Temperville (2010), Analytical approximate wave form for asymmetric waves, *Coastal Eng.*, *57*(7), 656–667, doi:10.1016/j.coastaleng.2010.02.005.

Bagnold, R. A. (1966), *An Approach to the Sediment Transport Problem From General Physics, Physiographic and Hydrolic Studies of Rivers, U.S. Geol. Surv. Prof. Pap.*, vol. 422, U.S. Govt. Print. Off., Washington.

Battjes, J. A., and J. P. F. M. Janssen (1978), Energy loss and set-up due to breaking of random waves, *Coastal Eng.*, *1*(16), 569–587.

Bertin, X., A. B. Fortunato, and A. Oliveira (2009a), A modeling-based analysis of processes driving wave-dominated inlets, *Cont. Shelf Res.*, *29*(5–6), 819–834, doi:10.1016/j.csr.2008.12.019.

Bertin, X., A. Oliveira, and A. B. Fortunato (2009b), Simulating morphodynamics with unstructured grids: Description and validation of a modeling system for coastal applications, *Ocean Modell.*, *28*(1–3), 75–87, doi:10.1016/j.ocemod.2008.11.001.

Bruneau, N., A. B. Fortunato, G. Dodet, P. Freire, A. Oliveira, and X. Bertin (2011), Future evolution of a tidal inlet due to changes in wave climate, sea level and lagoon morphology (Óbidas Lagoon, Portugal), *Cont. Shelf Res.*, *31*, 1915–1930, doi:10.1016/j.csr.2011.09.001.

Booij, N., R. C. Ris, and L. H. Holthuijsen (1999), A third-generation wave model for coastal regions: 1. Model description and validation, *J. Geophys. Res.*, *104*(C4), 7649–7666, doi:10.1029/98JC02622.

Cayocca, F. (2001), Long-term morphological modeling of a tidal inlet: The Arcachon Basin, France, *Coastal Eng.*, *42*(2), 115–142, doi:10.1016/S0378-3839(00)00053-3.

Colebrook, C. F., and C. M. White (1937), Experiments with fluid friction in roughened pipes, *Proc. R. Soc. London, Ser. A*, *161*(906), 367–381.

Dastgheib, A. (2012), Long-term process-based morphological modeling of large tidal basins, PhD thesis, CRC Press/Balkema, TU, Delft.

Dingemans, M. W., A. C. Radder, and H. J. de Vriend (1987), Computation of the driving forces of wave-induced currents, *Coastal Eng.*, *11*, 539–563, doi:10.1016/0378-3839(87)90026-3.

Dissanayake, D. M. P. K., J. A. Roelvink, and M. van der Wegen (2009), Modelled channel patterns in a schematized tidal inlet, *Coastal Eng.*, *56*(11–12), 1069–1083, doi:10.1016/j.coastaleng.2009.08.008.

Ehlers, J. (1988), *The Morphodynamics of the Wadden Sea*, A. A. Balkema Publ., Rotterdam.

Elias, E. P. L., J. Cleveringa, M. C. Buijsman, J. A. Roelvink, and M. J. F. Stive (2006), Field and model data analysis of sand transport patterns in Texel tidal inlet (the Netherlands), *Coastal Eng.*, *53*(5–6), 505–529, doi:10.1016/j.coastaleng.2005.11.006.

Fiechter, J., K. L. Steffen, C. N. Mooers, and B. K. Haus (2006), Hydrodynamics and sediment transport in a southeast Florida tidal inlet, *Estuarine Coastal Shelf Sci.*, *70*(1–2), 297–306, doi:10.1016/j.ecss.2006.06.021.

FitzGerald, D. M. (1982), Sediment bypassing at mixed energy tidal inlets, in *Proceedings of the 18th Coastal Engineering Conference*, vol. 1, edited by D. M. FitzGerald, pp. 1094–1118, ASCE, CApe Town, doi:10.9753/icce.v18.%p.

FitzGerald, D. M. (1988), Shoreline erosional-depositional processes associated with tidal inlets, in *Hydrodynamics and Sediment Dynamics of Tidal Inlets*, vol. 29, edited by D. G. Aubrey and L. Weishar, pp. 186–225, Springer, New York.

FitzGerald, D. M., N. C. Kraus, and E. B. Hands (2000), Natural mechanisms of sediment bypassing at tidal inlets, Tech. Rep., US Army Corps of Engineers, Vicksburg, Miss.

Fredsoe, J. (1984), Turbulent boundary layer in wave-current motion, *J. Hydraul. Eng.*, *110*(8), 1103–1120, doi:10.1061/(ASCE)0733-9429(1984)110:8(1103).

Gaudiano, D. J., and T. W. Kana (2001), Shoal bypassing in mixed energy inlets: Geomorphic variables and empirical predictions for nine South Carolina inlets, *J. Coastal Res.*, *17*(2), 280–291.

Grunnet, N. M., D. J. R. Walstra, and B. G. Ruessink (2004), Process-based modelling of a shoreface nourishment, *Coastal Eng.*, *51*(7), 581–607, doi:10.1016/j.coastaleng.2004.07.016.

Hands, E. B., and V. Shepsis (1999), Cyclic channel movement at the entrance to Willapa Bay, Washington, USA, in *Proceedings of the 4th International Symposium on Coastal Sediments*, edited by N. C. Kraus and W. G. McDougal, pp. 1522–1536, ASCE, Washington, D. C.

Hasselmann, K., et al. (1973), Measurements of wind-wave growth and swell decay during the Joint North Sea Wave Project (JONSWAP), *8*(12), 1–95.

Hayes, M. O. (1975), Morphology of sand accumulation in estuaries: An introduction to the symposium, in *Estuarine Research*, vol. 2, edited by L. E. Cronin, pp. 3–22, Acad. Press, New York.

Hayes, M. O., and D. M. FitGerald (2013), Origin, evolution, and classification of tidal inlets, *J. Coastal Res.*, *69*, 14–33, doi:10.2112/SI_69_3.

Herrling, G., and C. Winter (2014), Morphological and sedimentological response of a mixed-energy barrier island tidal inlet to storm and fair-weather conditions, *Earth Surf. Dyn.*, *2*, 363–382, doi:10.5194/esurf-2-363-2014.

Hoefel, F., and S. Elgar (2003), Wave-induced sediment transport and sandbar migration, *Science*, *299*(5614), 1885–1887, doi:10.1126/science.1081448.

Hofstede, J. L. A. (1999), Process-response analysis for Hornüm tidal inlet in the German sector of the Wadden Sea, *Quat. Int.*, *60*, 107–117, doi:10.1016/S1040-6182(99)00010-5.

Holthuijsen, L. H. (2007), *Waves in Oceanic and Coastal Waters*, Cambridge Univ., Netherlands.

Ikeda, S. (1982), Lateral bed load transport on side slopes, *J. Hydraul. Div.*, *108*(11), 1369–1373.

Isobe, M., and K. Horikawa (1982), Study on water particle velocities of shoaling and breaking waves, *Coastal Eng. Jpn*, *25*, 109–123.

Komen, G. J., K. Hasselmann, and K. Hasselmann (1984), On the existence of a fully developed wind-sea spectrum, *J. Phys. Oceanogr.*, *14*(8), 1271–1285, doi:10.1175/1520-0485(1984)014<1271:OTEOAF>2.0.CO;2.

Lesser, G. R., J. A. Roelvink, J. A. T. M. van Kester, and G. S. Stelling (2004), Development and validation of a three-dimensional morphological model, *Coastal Eng.*, *51*(8–9), 883–915, doi:10.1016/j.coastaleng.2004.07.014.

Lippman, T. C., and R. A. Holman (1990), The spatial and temporal variability of sand bar morphology, *J. Geophys. Res.*, *95*(C7), 11,575–11,590.

Longuet-Higgins, M. S., and R. W. Stewart (1962), Radiation stress and mass transport in gravity waves, with application to 'surf beats', *J. Fluid Mech.*, *13*, 481–504, doi:10.1017/S0022112062000877.

Nahon, A., X. Bertin, A. B. Fortunato, and A. Oliveira (2012), Process-based 2DH morphodynamic modeling of tidal inlets: A comparison with empirical classifications and theories, *Mar. Geol.*, *291*, 1–11, doi:10.1016/j.margeo.2011.10.001.

O'Connor, M. C., J. A. G. Cooper, and D. W. T. Jackson (2011), Decadal behavior of tidal inlet-associated beach systems, Northwest Ireland, in relation to climate forcing, *J. Sediment. Res.*, *81*, 38–51, doi:10.2110/jsr.2011.3.

Oertel, G. F. (1975), Ebb-tidal deltas of Georgia estuaries, in *Estuarine Research*, vol. 2, edited by L. E. Cronin, pp. 267–276, Acad. Press, New York.

Ranasinghe, R., and C. Pattiaratchi (2003), The seasonal closure of tidal inlets: Causes and effects, *Coastal Eng.*, *45*(04), 601–627, doi:10.1142/S0578563403000919.

Reniers, A. J. H. M., J. A. Roelvink, and E. B. Thornton (2004), Morphodynamic modeling of an embayed beach under wave group forcing, *J. Geophys. Res.*, *109*(C1), C01030, doi:10.1029/2002JC001586.

Ribas, F., A. Falques, H. E. de Swart, N. Dodd, R. Garnier, and D. Calvete (2015), Understanding coastal morphodynamic patterns from depth-averaged sediment concentration, *Rev. Geophys.*, *53*(2), 362–410, doi:10.1002/2014RG000457.

Ridderinkhof, W., H. E. de Swart, M. van der Vegt, and P. Hoekstra (2014), Influence of the back-barrier basin length on the geometry of ebb-tidal deltas, *Ocean Dyn.*, *64*(9), 1333–1348, doi:10.1007/s10236-014-0744-3.

Ridderinkhof, W., P. Hoekstra, M. van der Vegt, and H. E. de Swart (2016), Cyclic migration of sandy shoals on the ebb-tidal deltas of the Wadden Sea, *Cont. Shelf Res.*, *115*, 14–26, doi:10.1016/j.csr.2015.12.014.

Robinson, A. H. W. (1975), *Cyclic Changes in Shoreline Development at the Entrance to Teignmouth Harbour, Devon, England*, vol. 8, pp. 181–200, John Wiley, London, U. K.

Roelvink, J. A. (2006), Coastal morphodynamic evolution techniques, *Coastal Eng.*, *53*(2–3), 277–287, doi:10.1016/j.coastaleng.2005.10.015.

Roelvink, J. A., and D. J. R. Walstra (2004), Keeping it simple by using complex models, *Adv. Hydro. Sci. Eng.*, *6*, 1–11.

Roelvink, J. A., A. J. H. M. Reniers, A. van Dongeren, J. S. M. van Thiel de Vries, R. T. McCall, and J. M. Lescinski (2009), Modelling storm impacts on beaches, dunes and barrier islands, *Coastal Eng.*, *56*(11–12), 1133–1152, doi:10.1016/j.coastaleng.2009.08.006.

Ruessink, B. G., Y. Kuriyama, A. J. H. M. Reniers, J. A. Roelvink, and D. J. R. Walstra (2007), Modeling cross-shore sandbar behavior on the timescale of weeks, *J. Geophys. Res.*, *112*, F03010, doi:10.1029/2006JF000730.

Ruessink, B. G., G. Ramaekers, and L. C. van Rijn (2012), On the parameterization of the free-stream non-linear wave orbital motion in nearshore morphodynamic models, *Coastal Eng.*, *65*(0), 56–63, doi:10.1016/j.coastaleng.2012.03.006.

Sha, L. P., and J. H. van den Berg (1993), Variation in ebb-tidal delta geometry along the coast of the Netherlands and the German Bight, *J. Coastal Res.*, *9*(3), 730–746.

Siegle, E., D. A. Huntley, and M. A. Davidson (2004), Physical controls on the dynamic of inlet sandbar systems, *Ocean Dyn.*, *54*, 360–373, doi:10.1007/s10236-003-0062-7.

Soo Son, C., B. W. Flemming, and A. Bartholoma (2011), Evidence for sediment recirculation on an ebb-tidal delta of the East Frisian barrier-island system, southern North Sea, *Geo-Mar. Lett.*, *31*, 87–100, doi:10.1007/s00367-010-0217-8.

Soulsby, R. L., A. G. Davies, J. Fredsoe, D. A. Huntley, I. G. Jonnson, D. Myrhaug, R. R. Simons, A. Temperville, and T. J. Zitman (1993), Bed shear stresses due to combined waves and currents, in *Abstracts-in-depth of the Marine Science and Technology G8-M Overall Workshop*, pp. 2.1–1–2.1-4, European Commission, Grenoble, France.

Stelling, G. S., and J. J. Leendertse (1992), Approximation of convective processes by cyclic AOI methods, in *Estuarine and Coastal Modeling*, edited by M. L. Spaulding et al., pp. 771–782, ASCE, New York.

van der Wegen, M., and J. A. Roelvink (2008), Long-term morphodynamic evolution of a tidal embayment using a two-dimensional, process-based model, *J. Geophys. Res.*, *113*, C03016, doi:10.1029/2006JC003983.

van Rijn, L. C. (2007a), Unified view of sediment transport by currents and waves. I: Initiation of motion, bed roughness, and bed-load transport, *J. Hydraul. Eng.*, *133*(6), 649–667, doi:10.1061/(ASCE)0733-9429(2007)133:6(649).

van Rijn, L. C. (2007b), Unified view of sediment transport by currents and waves. II: Suspended transport, *J. Hydraul. Eng.*, *133*(6), 668–689, doi:10.1061/(ASCE)0733-9429(2007)133:6(668).

van Rijn, L. C., D. J. R. Walstra, and M. van Ormondt (2004), Description of TRANSPOR2004 and implementation in Delft3D-online, Tech. Rep. Z3748.10, Deltares (WL), DG Rijkswaterstaat, RIKZ, Delft, Netherlands.

Walstra, D. J. R., A. J. H. M. Reniers, R. Ranasinghe, J. A. Roelvink, and B. G. Ruessink (2012), On bar growth and decay during interannual net offshore migration, *Coastal Eng.*, *60*, 190–200, doi:10.1016/j.coastaleng.2011.10.002.

Walton, T. L., and W. D. Adams (1976), Capacity of inlet outer bars to store sand, in *Proceedings of the 15th Coastal Engineering Conference*, pp. 1919–1937, ASCE, Honolulu, Hawaii.